

Quantum Mechanical Arrival Time Distributions In Free Fall Experiments Across Opaque Barriers

May 2025

Adam Blazejczak^{1†}, Jef Hooyberghs², Siddhant Das³, Ward Struyve⁴

^{1,2†}UHasselt, Theory Lab, Agoralaan, 3590 Diepenbeek, Belgium

³LMU Munich, ASC for Theoretical Physics, Theresienstraße, 80333 München, Germany

⁴KU Leuven, Institute for Theoretical Physics, Celestijnenlaan, 3001 Leuven, Belgium

Keywords: quantum mechanics, Bohmian mechanics, arrival time, tunneling time, quantum free fall, gaussian barriers, larmor clock, split operator method, Yoshida method, spin precession

†Corresponding author. Tel: +32 485 974 525; E-mail address: adam@blvckstudios.com

ABSTRACT

Canonical quantum mechanics focuses on measurement outcomes, while alternative formulations like Bohmian mechanics describe the particle's path from A to B, while yielding the same predictions. In experiments like the double-slit, the concept of "travel time" or "arrival time" lacks precision due to issues with initial conditions. However, free-fall experiments with quantum particles on opaque barriers might resolve this. This study introduces an analysis of such setups, calculating arrival times using Bohmian probability currents at the detector location. The resulting distributions reveal band formation, tunneling resonances, and other features, suggesting further theoretical and experimental exploration. The study also compares tunneling times predicted by the Larmor clock for spin- $\frac{1}{2}$ particles and Bohmian mechanics. Both theories agree with square barriers, but show differences with Gaussian barriers, highlighting the ad hoc nature of the Larmor clock theory. Dutch version on page 14.

1 INTRODUCTION

Unlike in General Relativity, the notion of time in Quantum Mechanics is considered a

parameter, and no adequate **Time Operator** has been produced since physicists first started pondering the question in 1939 (see appendix 7.1 for a deeper treatment). Canonical quantum formalism seems to be particularly concerned with **measurement outcomes**, with less interest in the *journey* that a particle takes from its *conception* to its measurement. For instance, the famous interference pattern produced in the dual slit experiment is incredibly well described and predicts experimental outcomes adequately. To get a fuller picture of such an elementary experiment, however, the idea of "time of flight" of a quantum particle is required. The central question in this study resounds as follows:

When will a detector click?

The answer to this question is answered by the **Arrival Time Distribution** of a quantum system at some detector location or surface. For trivial systems with no barriers or scattering potentials, the mean arrival time can be estimated semiclassically as $\tau_{\text{arrival}} \simeq L/\langle v \rangle$, with $\langle v \rangle = \hat{p}/m$, but this approach breaks for even the most basic potentials and barriers. Canonical quantum mechanics can't answer this question, but in Bohmian Mechanics, an alternative formulation of quantum mechanics which holds the same predictive power as canonical formalisms, the arrival time *is* cal-

cutable and mainly justified by the theory's existence of **Bohmian trajectories**. In experiment, the arrival time has been measured for the double slit experiment using He atoms [1], whose results have been modelled and numerically reproduced using Bohmian Theory [2] [3]. An image of both can be found in figure 1. A clear "fanning out" of the arrival time has been observed and predicted, which after further analysis was due to an inherent uncertainty on the initial momentum p_0 of shot particles through the dual slits. This gave rise to the idea of conceiving a physically realizable experiment (using ultracold atoms and neutrons like in [4], [5], [6], and [7]) for which the initial conditions can be controlled exactly, allowing precise prediction and subsequent measurement of arrival time distributions in quantum mechanics. The answer to this question is answered by the **Arrival Time Distribution** of a quantum system at some detector location or surface. For trivial systems with no barriers or scattering potentials, the arrival time can be adequately described using semi-classical methods (via $m\langle v \rangle = \hat{H}\psi$). Canonical quantum mechanics can't answer this question, but in Bohmian Mechanics, an alternative formulation of quantum mechanics which holds the same predictive power as canonical formalisms, the arrival time *is* calculable and mainly justified by the theory's existence of **Bohmian trajectories**. In experiment, the arrival time has been measured for the double slit experiment using He atoms [1], whose results have been modelled and numerically reproduced using Bohmian Theory [2] [3]. An image of both can be found in figure 1. A clear "fanning out" of the arrival time has been observed and predicted, which after further analysis was due to an inherent uncertainty on the initial momentum p_0 of shot particles through the dual slits. This gave rise to the idea of conceiving a physically realizable experiment (using ultracold atoms (neutrons) like in [4], [5], [6], and [7]) for which the initial conditions can be controlled exactly, allowing precise pre-

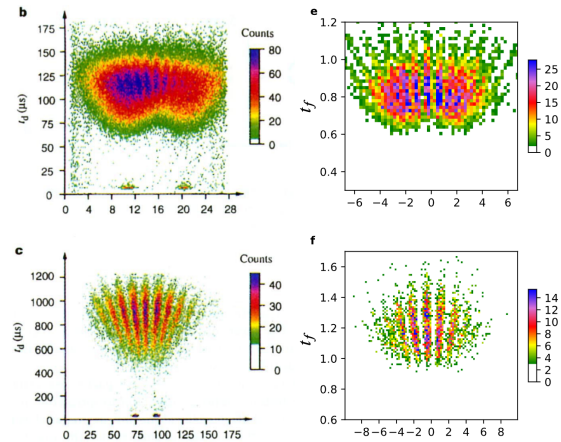


Figure 1: Figure showing arrival times of He atoms shod through a dual slit (left), and numerical predictions made using a Bohmian mechanics [2]

diction and subsequent measurement of arrival time distributions in quantum mechanics.

One such proposed experiment by our research group is putting a quantum particle at rest in free fall. The particle would fall onto a barrier, and a detector would be put below the barrier. The detector will measure the arrival time of the tunnelled component. Since the barrier will reflect a portion of the wave function back up, that portion would inevitably fall back down again due to the linear gravitation potential, giving rise to quantum mechanical arrival time distributions to be studied both experimentally, and theoretically.

Arrival time distributions of quantum particles falling onto Gaussian barriers under free fall has not yet been studied in literature, making this study an initial theoretical analysis of such setups.

The second part of this study focuses on **tunnelling time** of free-falling spin- $\frac{1}{2}$ particles onto magnetic Gaussian barriers, comparing Bütticker's Larmor Clock in the low magnetic regime with predictions made with Bohmian Formalism. A more thorough explication of the arrival time and tunnelling time in context

of literature can be found in appendix 7.2.

2 THEORY

The necessary theory for understanding the numerical procedures and results are briefly explicated.

2.1. Arrival Time

In a Bohmian Mechanical formalism, the wave function and Schrödinger equation are foundational, just like in canonical formalisms, yet particles are dot-like entities which are **guided** by a pilot wave, making particles have a definite velocity and **trajectory**. Have a general wave function be written as

$$\Psi = \sqrt{\rho(\vec{r}, t)} \cdot \exp\left(i \frac{S(\vec{r}, t)}{\hbar}\right), \quad (1)$$

where $\rho(\vec{r}, t) = \Psi^* \Psi$ is the probability density of the wave function, and $S(\vec{r}, t)$ its phase. One may now write the Bohmian velocity in the following form:

$$\vec{v} = \frac{\vec{j}(\vec{r}, t)}{\rho(\vec{r}, t)} = \frac{1}{m} \nabla S(\vec{r}, t), \quad (2)$$

where \vec{j} represents the probability current or **probability flux** of the wave function. The spatial variation of the wave function characterizes the probability flux of the wave function, and thus also its velocity. The arrival time of a particle in Bohmian Mechanics can be determined by following the motion of a particle's Bohmian trajectory, then registering the time at which the trajectory arrives at the detector:

$$\frac{d}{dt} \vec{r}(t) = \vec{v}(\vec{r}(t), t) = \frac{|j(\vec{r}(t), t)|}{|\Psi(\vec{r}(t), t)|^2} \quad (3)$$

$$\Rightarrow \vec{r} = \vec{r}_0 + \int_0^t \vec{v} dt \quad (4)$$

Using the concept of Bohmian trajectories, the arrival time is the average traversal time across all these trajectories, having the trajectories start at $|\psi_0|^2$, and arrive or cross a detector at an arbitrary path, plane or volume in the studied system (in this study, the detector). For this to hold,

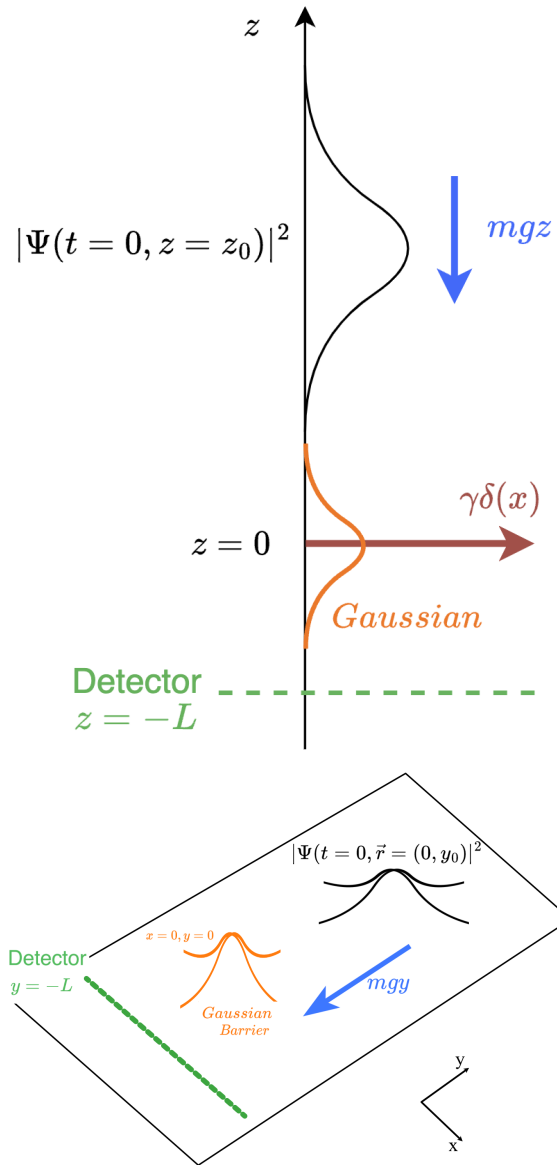


Figure 2: Setup of Gaussian Particle Falling onto a barrier in 1 dimension, with a detector present at $z = -L$. In this study, barriers of the delta type $\gamma\delta$ and Gaussian types are considered. The 2D setup is of similar nature to the 1D experiment, where the barrier represents a uniform magnetic field of a Gaussian amplitude profile pointing in the z direction.

special requirements ought to be taken into consideration: the probability current needs to be strictly positive, and hence **backflow** of the trajectories needs to be eliminated (more on this in appendix 7.3), or at least: only the first crossing of a trajectory needs to be considered. This is done by truncating the Bohmian trajectories (like in [2]), or by using complex absorption potentials (similar to Tumulka's approach in [8]) at the boundaries of the numerical simulation. Both approaches are employed in this text. In any case, Bohmian trajectories justify the notion of using probability currents to describe an arrival time distribution, since it concerns itself with the **realism** of quantum mechanical systems, as opposed to only the **outcomes** of measurements as in canonical formalisms. For this to work, the previously mentioned conditions need to be met, which are summarised in the following box:

The probability density of the arrival time t at a detector $\vec{r}_{\text{detector}}$ is given by:

$$\Pi(t) = -j(\vec{r}_{\text{detector}}, t) \quad (5)$$

iff the bohmian trajectories are strictly positive to one direction across the detector.

Studies [9] [10] have shown that no POVM nor PVM exists for which $\langle \psi_0 | \hat{O}_t | \psi_0 \rangle = j(x=0, t)$ holds generally, however, the conditions in the boxed results are met in the studied free-fall setup, making the numerical setup feasible and physically meaningful. For a deep dive into the reasoning and setup of the boxed equation, please see appendix 7.3. The appendix also contains results and comparison of analytical solutions to the studied setup for weak delta barriers.

2.2. Tunnelling Time

In the Bohmian Mechanical picture, tunnelling time through a barrier is adequately defined due to the nature of **Bohmian trajectories**, and follows the same argument as for the arrival time in the previous section. Consider the setup as seen in figure 3, where a nor-

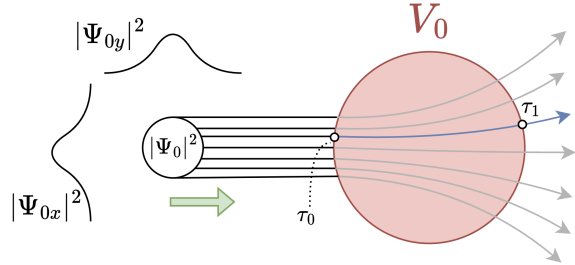


Figure 3: The tunnelling time on Bohmian trajectory is defined as $\tau_1 - \tau_0$, respectively the time of entering and exiting the barrier, in case the boundaries of the barrier are well-defined.

malized Gaussian wave packet ψ_0 approaches a potential V_0 . Consider a Bohmian trajectory $\vec{Q}(t)$, which tunnels through the barrier of strength V_0 . The tunnelling time of this trajectory equals to $\tau_Q = \tau_1 - \tau_0$, at least if the boundary of the barrier is well-defined. In the discussion section of this paper, it shall be discussed how Gaussian barriers have a not well-defined barrier, making the notion of tunnelling time inherently ambiguous in the Bohmian picture. In any case, the average tunnelling time of a quantum particle is the average tunnel time of N such Bohmian trajectories, which have been initialized in accordance to the wave function density distribution $|\psi_0|^2$:

$$\tau_t = \frac{1}{N} \sum_{i=0}^N \tau_1^{(i)} - \tau_0^{(i)} \quad (6)$$

Here too, backflow ought to be taken into consideration at the location of the idealised detector, and only the first crossing of the trajectory counts towards tunnelling time.

2.3. Larmor Spin Precession And Larmor Clocks

A classical electromagnetic result states that a dipole put in a uniform magnetic field B_0 will start precessing at the **Larmor frequency** due to the torque exerted on the dipole. This quantity is given by

$$\omega_L = \gamma B_0. \quad (7)$$

This classical result, applies to dipoles produced by quantum mechanical spin- $\frac{1}{2}$ particles. For electrons, $\gamma_e = -\frac{e}{2m_e}g_e$, with $g_e \approx 2$, the electron g-factor, and m_e the electron mass. For nuclei, $\gamma_n = \frac{e}{2m_p}g$, with g the nuclear g-factor, and m_p the proton mass. Bütticker argued in 1983 [11] that spin-precession can be used to retrieve the *dwell time* of a particle in a weak magnetic barrier, which is called the **Larmor Clock**. By shooting spin- $\frac{1}{2}$ particles through such magnetic fields, the expectation values of Pauli Spinors $\langle \sigma_x \rangle$ and $\langle \sigma_y \rangle$, in conjunction with the Larmor frequency, to retrieve an approximate **tunnelling time**. The main results are summarised in the box below:

$$\Theta(t) \approx \tan^{-1}\left(\frac{\langle \sigma_y \rangle}{\langle \sigma_x \rangle}\right) \quad (8)$$

$$\tau_{tunnelling} = \frac{\Delta\Theta}{\gamma B_0} = \frac{\Delta\Theta}{\omega_L} \quad (9)$$

Bütticker claimed that this result holds for any symmetric potentials of all kinds, in weak field regimes (including Gaussian ones) although the main derivation has been done using square potentials. The setup in this study assumes a uniform Gaussian magnetic field pointing in the positive z direction, which guarantees that the spin state remains in the xy-plane on the Bloch Sphere. **Larmor Clock** predictions are put against **Bohmian Tunnelling** predictions, and discussed. For a deeper treatment of the Larmor Clock, the reader is referred to appendix 7.5.

3 NUMERICAL PROCEDURES

All simulations are conducted in the **Python** programming language, in conjunction with the *numpy* [12] and *scipy* [13] numerical calculation packages. The computer used for running these simulations are listed in the table below:

Table 1: Specifications of simulation computer

Spec	Details
Model	MacBook Pro (14-inch, 2023)
Chip	Apple M2 Pro
CPU	10-core (6 at 3.5 Ghz - 2.4 Ghz)
Memory	32 GB
Storage	1 TB SSD

Simulations have been conducted using the **Split-Operator Method** which uses Fast Fourier Transforms (FFTs) for efficient time evolution of the TDSE with errors of order $\mathcal{O}(dt^3)$, as well as an $\mathcal{O}(dt^5)$ error extension, the **Yoshida Method** [14] for improved accuracy. A time step looks as follows, with \mathcal{F} and \mathcal{F}^{-1} resp. the discrete Fourier transformation and its reverse:

$$\psi(t + \Delta t) = e^{-\frac{i}{2\hbar}V\Delta t} \quad (10)$$

$$\mathcal{F}^{-1}[e^{-\frac{i\hbar k^2}{2m}\Delta t} \mathcal{F}[\psi(t)]] e^{-\frac{i}{2\hbar}V\Delta t}, \quad (11)$$

Both methods are compared. Since numerical simulations of quantum systems are done in a closed box environment, a complex absorption potential (CAP) is placed at 30% simulation units away from the edge, to ensure efficient absorption of the wave function, with no-to-minimal reflections. Grid searches are done in a reasonable range for dialling the free parameters of the Polynomial CAP. More CAPs mentioned in literature were tested, with the polynomial CAP working well for the purpose of this study. There's more information available in appendix 7.8. Finally, **spectral derivation** was employed to calculate Bohmian trajectories correctly. The main author found that the Bohmian velocity field were trailing behind the bulk of the $|\psi|^2$, possibly due to CFL conditions not being met [15]. Employing spectral derivation resolved this issue.

3.1. 1D Simulations

Spatial discretization. The coordinate axis is discretized by a uniform mesh $z_j = x_{\min} + j \Delta z$, $j = 0, \dots, N_x - 1$ with $\Delta z =$

$(x_{\max} - x_{\min})/N_x$. Derivatives entering the kinetic phase factor are evaluated in momentum space through the discrete Fourier transform, $k_j = 2\pi j/(N_x \Delta z)$, but in practice through the Fast Fourier Transform. Kinetic factors are calculated at each step using FFTs for quick iteration times. Picking $N_x = N_y = 1028$ with $\Delta t = 0.001s$ across $z \in [-40, 40]$ gave a good tradeoff between speed and physicality in produced simulation.

External potential. The total potential consists of a linear gravitational term, a tunable barrier at the origin, and an optional complex absorbing part,

$$V(z) = mgz + V_{\text{bar}}(z) - iW(z), \quad (12)$$

where $m = \hbar = 1$ and $g = 9.81$ in the simulation's natural units.

Barrier. Two barrier models are implemented in the simulation:

$$V_{\delta}(z) = \alpha \frac{\exp[-(z - z_0)^2/2\sigma^2]}{\sqrt{2\pi}\sigma}, \quad \sigma = \frac{1}{2}\Delta z, \quad (\text{"delta"})$$

$$V_g(z) = V_0 \exp[-(z - z_0)^2/2\sigma^2], \quad (\text{"gaussian"})$$

where the first line approximates an ideal δ -barrier by a narrow Gaussian whose width is tied to the grid spacing.

3.2. 2D Simulations with Spin

The setup for modelling Gaussian spin- $\frac{1}{2}$ particles falling under free fall throughout a magnetic is modelled by propagating a two-component spinor $\Psi(\mathbf{r}, t) = (\psi_{\uparrow}(\mathbf{r}, t), \psi_{\downarrow}(\mathbf{r}, t))^T$, $\mathbf{r} = (x, y)$, under a Hamiltonian that separates into kinetic and spin-dependent potential parts,

$$\hat{H} = \underbrace{\left[-\frac{\hbar^2}{2m} (\partial_x^2 + \partial_y^2) \right]}_{\hat{T} \otimes \mathbb{1}_{2 \times 2}} \quad (13)$$

$$+ \underbrace{\left[V_0(\mathbf{r}) \mathbb{1}_{2 \times 2} + V_B(\mathbf{r}) \sigma_z \right]}_{\hat{V}(\mathbf{r})} \quad (14)$$

where $V_0(\mathbf{r}) = mg y$ is the spin-independent gravitational term and $V_B(\mathbf{r})$ is a magnetic barrier that couples to the Pauli matrix σ_z . With the barrier centred at, (x_0, y_0) , a Gaussian profile is used for modelling a physically realistic laser profile

$$V_B^{(G)} = V_0^B \exp[-(\rho/\sigma)^2/2], \quad (15)$$

$$\rho^2 = (x - x_0)^2 + (y - y_0)^2, \quad (16)$$

or, in the second situation, a hard-edged circular uniform magnetic field B_0 . Both situations are compared.

The Split Operator Step in 2D requires more attention, with full details in appendix 7.11, although it follows the overall methodology as in 1D experiments. For 2D simulations, the number of memory required to complete a successful iteration grows exponentially. Careful memory management, and a discretization of $N_x = N_y = 512$ at a $\Delta t = 0.01s$ for a space of $x, y \in \mathbb{R}^2$ limited to $[-20, 20]$ works well for producing physically feasible simulations. The explored free parameter space explored in this study is listed in the appendix.

3.3. General Workflow

The overall workflows is briefly discussed for most simulations in this study. First, Siddant Das [16] low energy regime model for the arrival time distribution is compared with the setup numerical simulations. After this, the arrival time density for 1-dimensional simulations is analysed for different barrier strengths, different drop heights, and the arrival time peaks are characterized. Practise has shown that 1D simulations, across 400+ simulations with 50k time steps each, can be held in memory easily. The one dimensional arrival time calculations generally translate to two and three dimensions, due to the other dimensions not contributing non-trivially to the probability current at the plane $y = -L$, which can be removed from analysis by separation of variables. Next up, tunnelling time is analysed in the **Larmor Clock** theory and Bohmian Theory in 2D simulations. For this, two magnetic

barrier types are tested at different strengths (circular and Gaussian-profile uniform barriers). The simulation runs for 3 seconds, until the wave function hits the barrier. The simulated setup can be seen in figure 2 on page 3. For 2D data gathering, each simulation's data needs to be stored separately on file ($\approx 6.5\text{ Gb}$ per file), requiring about 450Gb in total storage for all 1D and 2D simulations made in this study. This storage space is readily available in the commercial laptop range. A single 2d simulation run takes ± 22 minutes, depending on available computer resources and simulation parameters. The general workflow for gathering quantities across many simulations is depicted in figure 12 on page 29.

4 RESULTS

Both 1D and 2D simulations across a wide range of parameters have been successfully performed. In figure 13 a single bounce of ψ across a strong barrier can be seen (1D). The wave function drops onto the barrier, is reflected upward, then drops again due to gravity. This process continues. The transmitted component is absorbed by the CAP and can be clearly seen in the image. Multiple bounces can be seen in figure 4 and a long-term run with a strong barrier can be seen in figure 14 on page 31. Calculated arrival time distributions across different barrier strengths can be seen in figure 16 on page 31, giving a clear representation of "arrival time peaks" at the detector.

4.1. $\mathcal{O}(dt^3)$ vs $\mathcal{O}(dt^5)$ Simulations

A few experiments across a wide range of parameters have been conducted to assess the difference in predicted arrival time distributions. Even for long runs (100+ s), the difference between the arrival time distributions doesn't exceed 1.75×10^{-8} in probability per unit time (PPT), on average, across the considered time domain. The first arrival time peak is impacted with the biggest error, hence the difference in first peak between both methods across a wide range of drop heights and

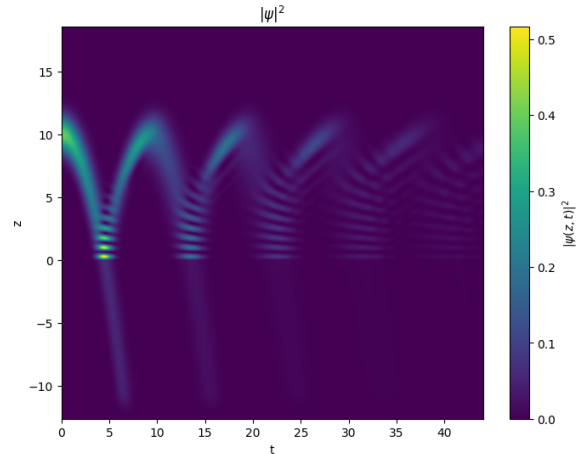


Figure 4: Showing $|\psi|^2$ of a quantum particle falling under free fall, the transmitted component is absorbed at the boundary of the simulation. The reflected part of the wave function falls back down to the barrier. A detector is placed at $z = -L = -5$

barrier strengths has been conducted, whose results can be seen in the heatmap in figure 5, an explicit difference plot between both methods can be found in the appendix.

The first peak error doesn't exceed more than 5×10^{-10} PPT, but given the sensitive nature of the analysis, all 1D simulations have been conducted with **Yoshida's method** for its improved accuracy.

4.2. Arrival Time Distributions

Delta-type and Gaussian-type Arrival Time distributions are run for different simulation parameters. The delta-type barriers seem to give classic-like arrival time distributions for different barrier strengths heights (figure 16 on page 31). Arrival times for Gaussian barriers clearly show *non-trivial* arrival time distributions.

This is most clearly noticeable by plotting the **arrival time distribution peaks**, focusing on their temporal distribution and intensity distribution across changing parameters, like barrier strength, and drop

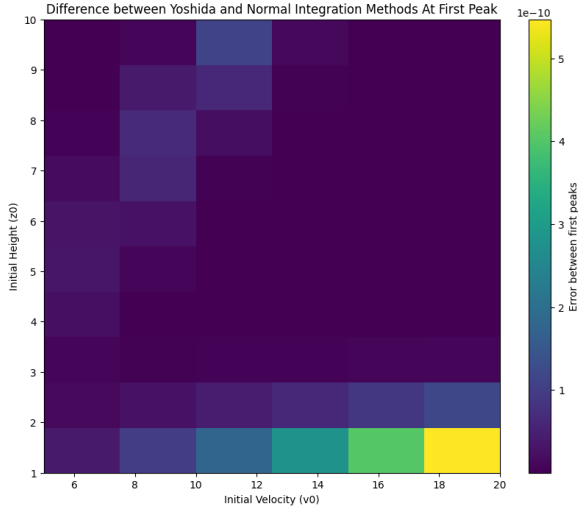
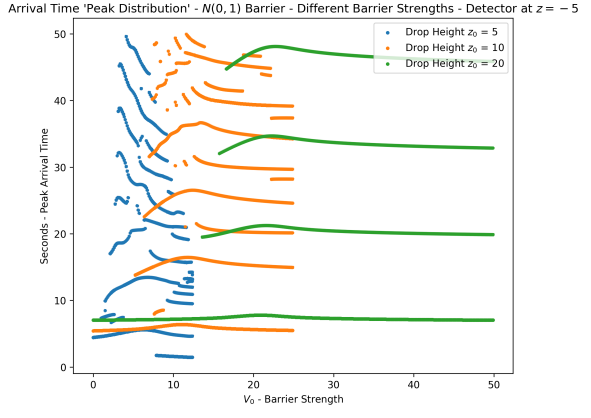


Figure 5: First Peak Difference in Arrival Time Density Between $\mathcal{O}(dt^3)$ and $\mathcal{O}(dt^5)$ methods

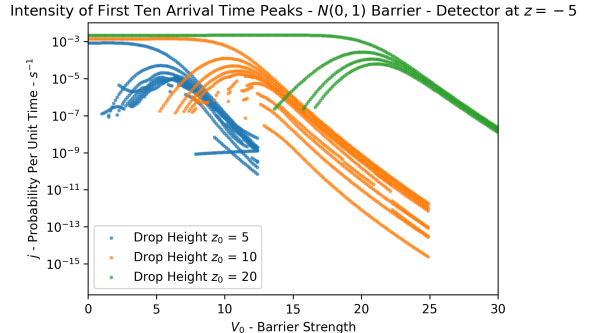
height. The main results can be compiled in figures 30 with more available in the appendix starting from page 32, including isolated cases for closer inspection of the intricate non-linear results.

4.3. Fitting Peaks

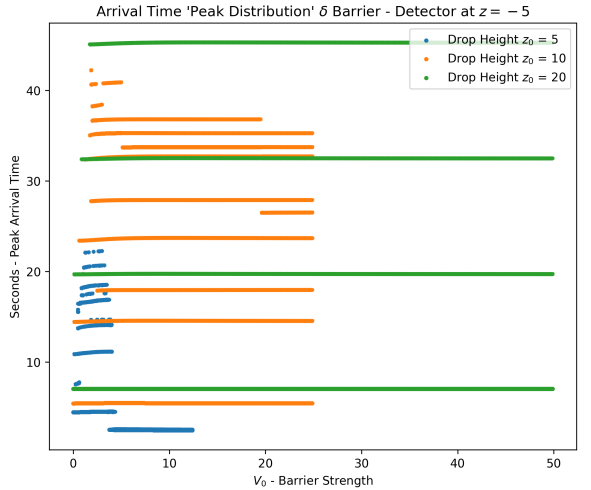
An interesting feature of the produced arrival time distributions is that their **peaks** look as if they are exponentially decaying over time. An attempt has been made to characterize the **decay constant** λ of these peaks. A clear linear correlation can be witnessed when plotting the arrival time peaks and its corresponding fit, on a logarithmic scale, as can be seen in figure 7. The retrieved reciprocal value for $\tau = \frac{1}{\lambda}$ are plotted for various drop heights z_0 and barrier strengths V_0 in figure 7, which includes error bars that represent $3000 \times$ the mean square error of the fit against the peaks. At least three peaks had to be identified for a fit to proceed, and peaks were identified as being local maxima, with intensities of at least 0.0001% of the first peak's PPT value (consistently the maximum intensity).



(a)



(b)



(c)

Figure 6: Arrival Time Distribution Peak times (a) and their corresponding intensities (b) are plotted in function of barrier strength V_0 : the dots in each vertical slice represent the peaks of the arrival time distribution. (c) represents arrival time peaks for a delta barrier.

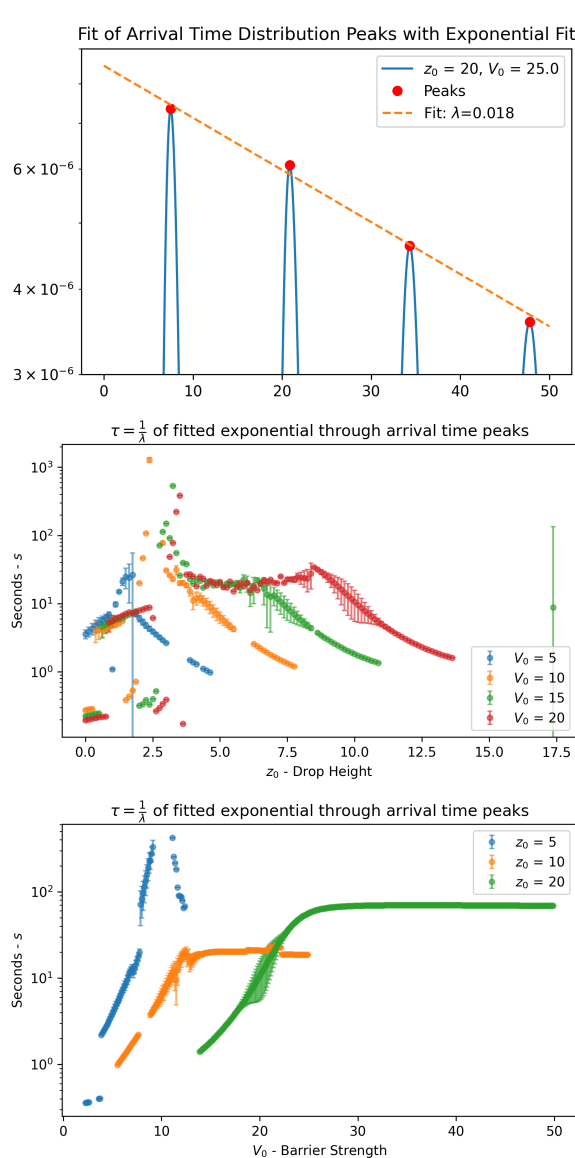


Figure 7: Value of fitted parameter $\tau = \frac{1}{\lambda}$ through arrival time peaks. Error bars represent mean square error times a constant factor 3000 to make them visible. The figure on top has units "Barrier Strength" on the x-axis, and "PPT" - Probability Per Unit Time on the y-axis. Missing τ values are indicative of no adequate fits, or absence of enough peaks (3) for fitting to proceed.

4.4. Tunnelling Time - Bohmian vs Larmor Clocks

With over $400 \times 2D$ simulations conducted, the tunnelling time using Bohmian trajectories and Larmor Clock Theory seem to coincide in the weak field regime, for circular barriers: $\tau_{\text{larmor}} = 0.172 \pm 1.51 \times 10^{-6}$ and $\tau_{\text{bohm}} = 0.170 \pm 2.77 \times 10^{-17}$ across the considered weak field range and setup parameters.

Bohmian Tunnelling time for Gaussian barriers seems to be problematic, mainly because it has no well-defined boundary, making boundary choice arbitrary. The Larmor Clock read $\tau = 0.574 \pm 7.81 \times 10^{-8} s$ across the weak field region. The tunnelling times are plotted against one other in figure 26 with strong field simulations and tunnelling time results available in the appendix on page fig:abc67rtyfugjop. To make the Bohmian trajectories coincide with Larmor clock time, the width of the boundary for counting Bohmian trajectories ought to be considered at $2R = 2.51\sigma$, which is just a little bit wider than the FWHM of a Gaussian, the experimentalist's definition of a typical laser width. This value was fitted using basic numeric iterations.

5 DISCUSSION

5.1. Arrival Time

The Arrival Time Distributions produce very interesting patterns, which resemble aspects of band theory in the weak barrier strength region, and regular patterns in higher barrier and energy strengths. The delta barrier arrival time peaks *seem* to be separated semiclassically which is expected, but a thorough theoretical treatment is in order to confirm this. For the Gaussian barrier, non-linear effects become apparent: there seems to be resonant energies at which tunnelling occurs, which is a quantum-typical effect. Higher drop heights of the quantum particle (higher energy particles), and stronger barriers, seem to produce stable and evenly spaced arrival time peaks and intensities, whereas the opposite (low energy) region is prone to strong non-linear effect, due

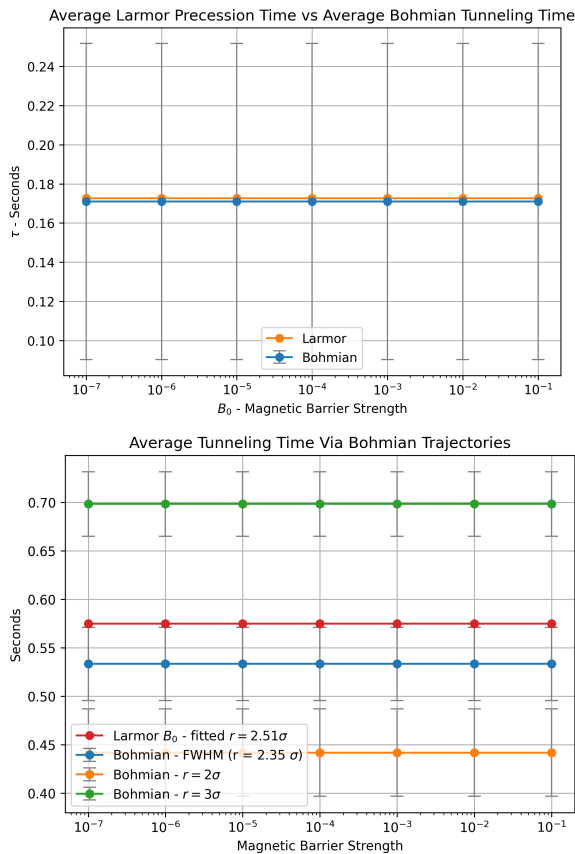


Figure 8: Tunnelling Times For a Circular Uniform Barrier with a clear boundary (a), and a Gaussian barrier (b) both using Larmor Precession Times τ_L , and Bohmian trajectories. These data points are obtained in the weak field regime. At low magnetic strengths, the two seem to coincide. Error bars on the Bohmian tunnelling time represent 1 standard deviation over the average Bohmian trajectory ensemble.

to tunnelling through a Gaussian barrier. In figure 20 on page 33, one may observe that the arrival time of the particles increases linearly with drop height, which is to be expected, yet the second, third, etc... peak, tend to stay longer above the barrier than at lower energies. This too suggests resonant tunnelling effects that have a direct impact on the arrival time distribution. The intensity distribution of arrival time peaks across different parameters generally follow intuition: less arrival intensity at every subsequent peak. Asymptotic exponential decreases in PPT are observed in the strong barrier region.

Peak Fitting. Some arrival time distributions (particularly those with strong barriers, and high drop heights) seem to produce linearly fittable peaks, yet at weaker regimes, are clearly less linear. The capacity for characterization of **arrival time peaks** using an exponentially decaying function would imply that $\tau = \frac{1}{\lambda}$ characterizes the **mean dwelling time** of the wave function above the barrier, since the time of arrival $\tau_{\text{detection}}$ is composed of $\tau_{\text{free}1} + \tau_{\text{tunnel}} + \tau_{\text{free}2}$. However, when considering figure 7, it's clear that fitted peaks ought to be considered more carefully: some peaks might be first order peaks (reflections from the positive side of the barrier), and second order peaks (reflections from the negative side of the barrier), which probably reflects in a spectrum of k -values, producing the observed non-linear effects, and very chaotic fitted $\frac{1}{\lambda}$ values (see error margins). The convergence of the fitted $\tau = \frac{1}{\lambda}$ in the strong barrier regions suggests a particle that keeps on dwelling above the barrier, never arriving at the detector at $y = -L$.

5.2. Larmor Clock vs Bohmian Tunnelling Time

Bohmian tunnelling time defines an exact average time a particle passes through a tunnel, a notion that is rejected in canonical quantum formalism, seems to coincide almost exactly with the **Larmor Clock** theory when the barrier is well-defined. Gaussian barriers,

however, are non-zero across their whole domain, making it impossible to define when a barrier begins, or when a wave function enters the barrier, since both are non-zero everywhere. Büttiker further argued that the Larmor Clock only works in weak magnetic fields, which has been confirmed in produced numerical methods under free-falling conditions. Where the weak field regime fails, Bohmian mechanics provides a straightforward and stable answer. It's experimentally impossible to measure whether a particle followed a Bohmian path or not, since the formalism is bound to measurement outcomes either way. Büttiker demonstrated theoretically that the Larmor Clock works for symmetrical non-uniform barriers, like Gaussians, which would imply that under Bohmian mechanical analysis, a Gaussian barrier has an effect radius $2R_{eff} = 2.51\sigma$, with σ being the standard deviation of a Gaussian laser profile, although more numerical experiments are in order for different barrier widths, shapes, and particle drop heights. Fundamentally speaking, the **Larmor Clock** is an ad hoc measure of time from fundamental quantities like spin, making the Larmor Clock a derivative quantity and ultimately debatable in its true meaning, as was also suggested by Sokolovski in [17].

6 CONCLUSION

Bohmian mechanical treatment of arrival time distributions for free-falling particles across opaque barriers have been successfully simulated using the Split Operator Method and its fourth order extension. The arrival time distribution has been obtained, giving interesting and non-trivial quantum-typical results like suggestions of band formation, tunnelling resonances, and quasi-stable standing wave formations. Tunnelling times using Larmor Clocks and Bohmian theory produce the same values when the boundary is well-defined in weak magnetic fields. For Gaussian profiles, tunnelling times do not coincide between the theories, due to lack of well-defined boundaries, and possible category errors when fundamen-

tally considering the classically defined **Larmor Spin Precession** in a quantum mechanical context.

Outlook. The first numerical analysis of the proposed experiment has been conducted, and experimentalists can now engage with the setup and provide invaluable data to engage in the fundamental study of arrival time, and the investigation of gravitational linearity at the quantum scale. Further, a proper theoretical treatment is in order, classifying, characterizing, and perhaps even properly predicting and explaining the arrival peak times observed in the simulations done in this study.

Author contributions

Adam Blazejczak wrote the code and scripts for simulating the 1D and 2D TDSE in python, has researched methods for improving numerical calculations, and came up with creative ways to analyse the resulting data. Adam also wrote this thesis from the ground up. **Ward Struyve, Siddhant Das** and their respective groups came up with the idea for analysing the free fall experiment across opaque barriers, to account for initial conditions. They also provided invaluable insight into Bohmian Mechanics. **Jef Hooyberghs** contributed to the interpretation, presentation and coherence of the thesis.

Acknowledgements

I would like to thank all my friends, peers, and colleagues who have supported me mentally and emotionally during my bachelor degree in physics at a mature age. I also would like to thank all members of the faculty at **HasseLT University** and **KU Leuven** for joining forces in creative ways, to deliver an impeccable learning experience and initiation into physics study, for young and older students alike.

Data And Code

The code for producing the results and data in this study are made available (starting from 27th May 2025) at <https://github.com/adamblvck/quantum-arrival-time-bachelor-thesis>. In case the repository wouldn't be available, please write an email to the corresponding author.

REFERENCES

- [1] Ch Kurtsiefer, Tilman Pfau, and Jürgen Mlynek. "Measurement of the Wigner function of an ensemble of helium atoms". In: *Nature* 386.6621 (1997), pp. 150–153.
- [2] Siddhant Das et al. "Double-slit experiment revisited". In: *Annals of Physics* (2025), p. 170054. ISSN: 0003-4916. DOI: <https://doi.org/10.1016/j.aop.2025.170054>. URL: <https://www.sciencedirect.com/science/article/pii/S003491625001356>.
- [3] Siddhant Das et al. "Double-slit experiment remastered". In: *arXiv preprint arXiv:2211.13362* 11 (2022).
- [4] Martin Robert De Saint Vincent et al. "A quantum trampoline for ultra-cold atoms". In: (2009). arXiv: 0911.0203 [physics.atom-ph]. URL: <https://arxiv.org/abs/0911.0203>.
- [5] Pascal Debu. "GBAR: Gravitational behavior of antihydrogen at rest". In: *Hyperfine Interact.* 212.1-3 (2012), pp. 51–59. DOI: [10.1007/s10751-011-0379-4](https://doi.org/10.1007/s10751-011-0379-4). URL: <https://cds.cern.ch/record/2861358>.
- [6] M.A. Zakharov et al. "A new approach to the experiment intended to test the weak equivalence principle for the neutron". In: *Journal of Physics: Conference Series* 746 (Sept. 2016), p. 012050. ISSN: 1742-6596. DOI: [10.1088/1742-6596/746/1/012050](https://doi.org/10.1088/1742-6596/746/1/012050). URL: <http://dx.doi.org/10.1088/1742-6596/746/1/012050>.
- [7] G.V. Kulin et al. "Spectrometer for new gravitational experiment with UCN". In: *Nuclear Instruments and Methods in Physics Research Section A: Accelerators, Spectrometers, Detectors and Associated Equipment* 792 (2015), pp. 38–46. ISSN: 0168-9002. DOI: <https://doi.org/10.1016/j.nima.2015.04.009>. URL: <https://www.sciencedirect.com/science/article/pii/S0168900215004684>.
- [8] Roderich Tumulka. "Distribution of the time at which an ideal detector clicks". In: *Annals of Physics* 442 (2022).
- [9] J.G. Muga and C.R. Leavens. "Arrival time in quantum mechanics". In: *Physics Reports* 338.4 (2000), pp. 353–438. ISSN: 0370-1573. DOI: [https://doi.org/10.1016/S0370-1573\(00\)00047-8](https://doi.org/10.1016/S0370-1573(00)00047-8). URL: <https://www.sciencedirect.com/science/article/pii/S0370157300000478>.
- [10] Nicola Vona, Günter Hinrichs, and Detlef Dürr. "What Does One Measure When One Measures the Arrival Time of a Quantum Particle?" In: *Physical Review Letters* 111.22 (Nov. 2013). ISSN: 1079-7114. DOI: [10.1103/physrevlett.111.220404](https://doi.org/10.1103/physrevlett.111.220404). URL: <http://dx.doi.org/10.1103/PhysRevLett.111.220404>.
- [11] Markus Büttiker. "Larmor Precession and the Traversal Time for Tunneling". In: *Physical Review B* 27.10 (1983), pp. 6178–6188. DOI: [10.1103/PhysRevB.27.6178](https://doi.org/10.1103/PhysRevB.27.6178).
- [12] Charles R. Harris et al. "Array programming with NumPy". In: *Nature* 585.7825 (Sept. 2020), pp. 357–362. DOI: [10.1038/s41586-020-2649-2](https://doi.org/10.1038/s41586-020-2649-2). URL: <https://doi.org/10.1038/s41586-020-2649-2>.
- [13] Pauli Virtanen et al. "SciPy 1.0: Fundamental Algorithms for Scientific Computing in Python". In: *Nature Methods* 17 (2020), pp. 261–272. DOI: [10.1038/s41592-019-0686-2](https://doi.org/10.1038/s41592-019-0686-2).
- [14] Haruo Yoshida. "Construction of higher order symplectic integrators". In: *Physics Letters A* 150.5-7 (1990),

- pp. 262–268. DOI: [10.1016/0375-9601\(90\)90092-3](https://doi.org/10.1016/0375-9601(90)90092-3).
- [15] R. Courant, K. Friedrichs, and H. Lewy. “On the Partial Difference Equations of Mathematical Physics”. In: *IBM Journal of Research and Development* 11.2 (1967), pp. 215–234. DOI: [10.1147/rd.12.0215](https://doi.org/10.1147/rd.12.0215).
- [16] Siddhant Das. “Tunneling through a thin potential barrier in free fall”. In: 2022.
- [17] D. Sokolovski and E. Akhmatkaya. “Tunnelling times, Larmor clock, and the elephant in the room”. In: *Scientific Reports* 11.1 (2021), p. 10040. ISSN: 2045-2322. DOI: [10.1038/s41598-021-89247-8](https://doi.org/10.1038/s41598-021-89247-8). URL: <https://doi.org/10.1038/s41598-021-89247-8>.
- [18] Wolfgang Pauli. *General Principles of Quantum Mechanics*. Springer Science Business Media, Reprint, 1986.
- [19] Eric A. Galapon. “Pauli’s Theorem and Quantum Canonical Pairs: The Consistency Of a Bounded, Self-Adjoint Time Operator Canonically Conjugate to a Hamiltonian with Non-empty Point Spectrum”. In: (2002).
- [20] Lorenzo Maccone Juan Leon. “The Pauli Objection”. In: (2024). URL: https://arxiv.org/html/1705.09212?utm_source=chatgpt.com.
- [21] Detlef Dürr Nicola Vona. “The role of the probability current for time measurements”. In: (2013).
- [22] E.J. Heller. “Time-dependent approach to semiclassical dynamics”. In: *The Journal of Chemical Physics* 62 (1975).
- [23] Siddhant Das and Detlef Dürr. “Arrival Time Distributions of Spin-1/2 Particles”. In: *Scientific Reports* 9.1 (2019), p. 2242. ISSN: 2045-2322. DOI: [10.1038/s41598-018-38261-4](https://doi.org/10.1038/s41598-018-38261-4). URL: <https://doi.org/10.1038/s41598-018-38261-4>.
- [24] R. Ramos - D. Spierings - I. Racicot - A. M. Steinberg. “Time-dependent approach to semiclassical dynamics”. In: *Nature* 583 (2020).
- [25] C. Cohen-Tannoudji, B. Diu, and F. Laloë. *Quantum Mechanics, Volume 1*. Wiley, 1977.
- [26] D. J. Griffiths and D. F. Schroeter. *Introduction to Quantum Mechanics*. 3rd ed. Cambridge University Press, 2018.
- [27] Detlef Dürr and Stefan Teufel. *Bohmian Mechanics: The Physics and Mathematics of Quantum Theory*. Berlin, Heidelberg: Springer, 2009. ISBN: 978-3-540-89343-1. DOI: [10.1007/b99978](https://doi.org/10.1007/b99978). URL: <https://link.springer.com/book/10.1007/b99978>.
- [28] Detlef Dürr, Sheldon Goldstein, and Nino Zanghì. *Quantum Physics Without Quantum Philosophy*. Berlin, Heidelberg: Springer, 2013. ISBN: 978-3-642-30690-7. DOI: [10.1007/978-3-642-30690-7](https://doi.org/10.1007/978-3-642-30690-7). URL: <https://books.google.be/books?id=LpnwCJfU-54C>.
- [29] C. R. Leavens and G. C. Aers. “A Local Version of the Larmor Clock”. In: *Solid State Communications* 67.12 (1988), pp. 1135–1143. DOI: [10.1016/0038-1098\(88\)91071-X](https://doi.org/10.1016/0038-1098(88)91071-X).
- [30] Michael D. Feit, J. A. Fleck, and A. Steiger. “Solution of the Schrödinger Equation by a Spectral Method”. In: *Journal of Computational Physics* 47.3 (1982), pp. 412–433. DOI: [10.1016/0021-9991\(82\)90091-2](https://doi.org/10.1016/0021-9991(82)90091-2).

ABSTRACT - DUTCH VERSION

Canonieke kwantummechanica richt zich op meetuitkomsten, terwijl alternatieve formuleringen zoals de Bohmse mechanica het volledige traject van een deeltje van A naar B beschrijven en toch identieke voorspellingen opleveren. In experimenten zoals het dubbelspleetexperiment ontbreekt echter een nauwkeurige definitie van ‘reistijd’ of ‘aankomsttijd’ wegens problemen met de beginvoorwaarden. Vrijevalsexperimenten met kwantumdeeltjes op niet-klassieke barrières kunnen dit vraagstuk mogelijk oplossen. Dit onderzoek introduceert een analyse van dergelijke opstellingen en berekent aankomsttijden via Bohmse kansstromen op de locatie van de detector. De resulterende verdelingen tonen bandvorming, tunnelresonanties en andere quantum kenmerken, wat uitnodigt tot verder theoretische behandelingen, en experimenteel onderzoek. Daarnaast worden de tunneltijden die de Larmor-klok voor deeltjes met spin $\frac{1}{2}$ voorspelt vergeleken met die uit de Bohmse mechanica. Beide theorieën komen overeen voor vierkante barrières, maar vertonen verschillen bij Gaussische barrières, een aanwijzing voor het ad hoc karakter van de Larmor-kloktheorie.

7 APPENDIX A - MORE DETAILS**7.1. Brief context of Time Operators**

In early quantum theory, time was treated as an external classical parameter, rather than a quantum observable. Unlike the position operator \hat{x} or the momentum operator \hat{p} , time doesn't currently have an adequate self-adjoint **time operator** in quantum formalism. Historically, Wolfgang Pauli has formulated this asymmetry with **Pauli's No-Go Theorem** (1933), stating that if a time operator \hat{T} would exist that is canonically conjugate to the Hamiltonian \hat{H} , satisfying the commutation relation

$$[\hat{T}, \hat{H}] = i\hbar \quad (17)$$

then the spectrum of the Hamiltonian must span the entire real domain, with the implication that the spectrum is **unbounded** both above and below, meaning that there would be no maximum nor minimum energy in the spectrum. For bounded particle this implies that they could exhibit arbitrarily negative energies, which contracts real-world systems that have empirically a measurable ground state. For Free particles on the other hand, with $\hat{H} = \frac{\hat{p}^2}{2m}$, are defined only for non-negative energies (these are bounded below), which correspond to observations in laboratories, and thus violate the consequences of Pauli's No-Go Theorem [18] [19].

Neither in literature, nor on Reddit, have an adequate and satisfactory time operator has been published or suggested thus far. However, under modern treatments it is possible to produce non-self adjoint operators which *act* like time operators. This usually involves careful considerations of highly specific cases, rather than generalizations [19]. Introducing quantum clocks, as part of the considered Hamiltonian system, through so called PWAK mechanisms [20] also seem to circumvent the

limitations paused by Pauli's Theorem. Modern approaches involve analysis and simulations of **Positive Operator-Valued Measures** (POVMs), which are suitable for outputting strictly positive probability distributions.

Their analysis usually involves considerations of quantum mechanical probability currents like in [21], or using absorbing boundaries like in [8].

7.2. Arrival Time and Tunnelling Time in Free Fall Experiments

Even though an adequate **Time Operator** has not yet been produced, characteristic times of experiments are being measured routinely in laboratories (see table 2). In this paper, focus has been put on asking the following central question:

When will a detector click?

The answer to this question is answered by the production of an **arrival time** distribution for a given setup. Of course, physics heralds its predictive and powerful legacy in both theoretical prediction and experimental verification. When no barriers or potentials are present in the time evolution of a quantum mechanical system, semi-classical approaches are exceedingly accurate for predicting the probability of arrival time [22]. In this paper, however, tunnelling and potential barriers are taken into consideration.

Perhaps most importantly, one ought to take the initial conditions of particles into consideration - the initial position and momentum of a particle have an inherent spread due to the uncertainty principle, making the arrival time inherently ambiguous. This is especially the case when *shooting* particles, as is done in most experiments.

For precise measurements of the arrival time, one way to tackle this is to consider a **physically realizable experiment** where

a particle in rest is released in free fall onto a barrier. A detector is placed below the barrier. In this setup, the particle will fall onto the barrier, part of it will reflect, and another part will transmit. The reflected portion of the particle will fall back onto the barrier due to linear gravitational potential. See figure 2 on page 3 for the setup of this experiment. When considering a delta barrier in specific far-field regimes, the arrival time can be approximated via the probability current, this is further discussed and argued in the theory section ahead, which has a Bohmian Mechanical justification for it.

The expected arrival times of particles falling onto gaussian barriers under free fall has not yet been conducted, making this study an initial theoretical analysis of such setups

Even though this will be explicated later in the theory section, it's interesting to note ahead that the Broglie-Bohm Pilot Wave Theory, or shortly **Bohmian Mechanics**, makes exactly the same predictions as the wave function formalism of quantum mechanics, but poses that quantum particles are dot like entities which follow a well-defined pathway, guided by a pilot wave (or quantum potential Q). Since the predictions are 1-to-1 with the canonical wave function formalism, the realism aspect of Bohmian Mechanics become interesting insofar as being unambiguous when considering the arrival time of quantum particles. Even more shockingly, it seems that Bohmian Mechanics poses the only unambiguous solution towards answering the question of arrival time, even though it's generally not accepted in canonical quantum formalism [23].

A second central question considered in the study is

How long does a particle spend in a barrier?

The answer to this question is answered by the prediction and measurement of **tun-**

tunnelling time. For a substantial period, physicists have considered barrier time to be superluminal (being faster than light). For instance, in 1980s the discussion has shifted to the consideration of "interaction time" of a particle with a barrier. Experiments have shown that *group delay* (phase time, or Wigner Time) is in fact superluminal in nature, however tunnelling time itself has been measured to be finite [24]. Ramos et Al in [24] have studied this by tunnelling Bose-condensed ^{87}Rb atoms through a $1.3\mu\text{m}$ optical barrier. By measuring **Larmor spin precession** of spin- $\frac{1}{2}$ particles through this barrier, via the classically derived Larmor Frequency ω_L , they arrived a tunnelling time as a derived quantity, and hence the time it took for the particle to cross the classically forbidden region. The measurement of spin precession usually involves setting up Stern-Gerlach experiments after passing a barrier. This approach is often called the **Larmor Clock** approach in literature, which is a classical approach to a quantum mechanical regime.

In this paper, the Larmor Clock approach is compared with predictions made by Bohmian Theory by means of numerical simulations, since the TDSE is analytically unsolvable but for the most basic potentials [25] [26]. The **tunnelling time** $\tau_{\text{tunnelling}}$ predicted by the two approaches are compared, analyzed, and scrutinized. The two theoretical frameworks are analysed on first principles basis as well in the discussion section. For simplicity of setup, this last approach is similar to the aforementioned setup: a particle (spin- $\frac{1}{2}$ this time) in rest is dropped in free fall, onto a **uniform magnetic barrier**. The expectation values of Pauli Spinors $\langle \sigma_x \rangle$ and $\langle \sigma_y \rangle$ are calculated and transformed into a spin precession calculation. This value for **tunnelling time** is compared to what a **bohmian view** would predict by the calculation of bohmian trajectories for the same quantum particle in the same setup through a magnetic barrier. The bohmian

tunnelling time is numerically by following the guiding pilot wave Q throughout the barrier.

The following theory section will expand on theoretical ideas and frameworks, including methods for numerically simulation of quantum mechanical systems.

7.3. Arrival Time

This section starts by considering the arrival time in quantum mechanical systems, the explanation is adapted from [21], omitting the semi-classical approach in this discussion. The discussion starts with the canonical quantum formalism, after which the shift towards Bohmian mechanics is made.

7.3.1. Arrival Time From a Canonical Perspective

Consider a particle that crosses a detector at time t' with 100% certainty. This implies that the particle was on one side of the detector before t' , and on the other side after t' , which leads to a good reason to connect arrival time statistics with the probability that a particle is on one side of the detector at different times. Consider the easiest possible case, depicted in figure 9, a one dimensional free particle is placed on the positive real half-line, moving towards the origin, with strict negative momentum:

$$\psi_0(x, t = 0) \approx 0 \quad \forall x \leq 0 \quad (18)$$

$$\tilde{\psi}_0(p, t = 0) = 0 \quad \forall p \geq 0 \quad (19)$$

With $\tilde{\psi}$ the Fourier transformed of ψ_0 . Having a strict negative momentum, the particle is guaranteed to cross the origin, and thus cross the detector from right to left. In this situation, having the particle cross the origin at time t' , it's not far-fetched to think that the probability to have the particle cross the origin at a time $\tau > t'$, is the probability of finding the particle still in the positive region at time t' :

Table 2: Characteristic times

Time	Name	Description
τ_L	Lifetime	Usual lifetime for decay, $\hbar/2\pi\rho(E) \langle f H i\rangle ^2$
τ_Z	Zeno time	Inverse of energy spread, $\hbar/\sqrt{\langle\psi (H-E_\psi)^2 \psi\rangle}$
τ_J	Jump time	τ_Z^2/τ_L
τ_T	Tunnelling time	Time spent in barrier
$\tau_A = \Pi$	Arrival time	Time of arrival at a detector
τ_P	Passage time	Minimum time to go from a state to a \perp one, $\pi\tau_Z/2$
τ_R	Response time	A property of monitoring apparatus
τ_{PM}	Pulse time	Interval between ideal pulsed measurements (cf. QZE)
τ_{Door}	Door time	Metaphorical

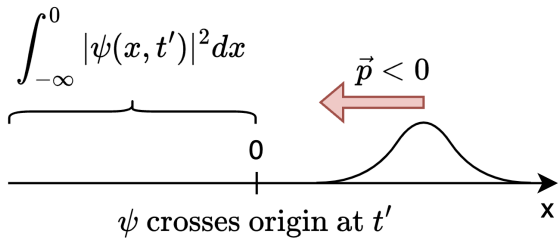


Figure 9: A simple setup for discussing arrival time. The particle has a strictly negative momentum and moves towards the origin where a detector sits

$$\Pi(t) = \frac{d}{dt} P(\tau < t) \quad (24)$$

$$= \int_{-\infty}^0 \frac{\partial}{\partial t} |\psi(x, t)|^2 dx \quad (25)$$

Because solutions to the Schrödinger equation are subject to the **probability continuity equation**, which states that:

$$\frac{\partial}{\partial t} |\psi(x, t)|^2 + \frac{\partial}{\partial x} j(x, t) = 0 \quad (26)$$

with $j(x, t)$ the probability current defined as:

$$P(\tau \geq t') = P(x \geq 0, t = t') \quad (20)$$

$$= \int_0^\infty |\psi(x, t = t')|^2 dx \quad (21)$$

$$j(x, t) = \frac{\hbar}{m} \operatorname{Im} \left(\psi^* \frac{\partial}{\partial x} \psi \right) \quad (27)$$

On the other hand, the probability to have the particle cross the detector before t' is:

$$P(\tau < t') = 1 - P(\tau > t') \quad (22)$$

$$= \int_{-\infty}^0 |\psi(x, t = t')|^2 dx \quad (23)$$

Hence, the probability density $\Pi(t)$ for crossing the detector at time t is given by, substituting $t' \rightarrow t$:

$$\Pi(t) = \frac{d}{dt} P(\tau < t) \quad (28)$$

$$= - \int_{-\infty}^0 \frac{\partial}{\partial x} j(x, t) dx \quad (29)$$

$$= -j(x = 0, t) + j(x = -\infty, t) \quad (30)$$

$$= -j(x = 0, t) \quad (31)$$

This gives the following result:

The probability density of the arrival time t at a detector in the origin, is given by the probability current at the origin.

$$\Pi(t) = -j(x = 0, t) \quad (32)$$

The boxed result only works when the **probability current is strictly negative, which cannot be generally guaranteed**, even though the momentum was strictly negative in the setup. A strictly negative momentum implies that the momentum would be measured strictly negative. Before measurement there's no sense of speaking of a particle's position, nor momentum, therefore there's no way of conceiving how a particle moves in the system in this framework. In canonical quantum formalism, it's unwarranted to claim that a particle will only *moves one time* from the negative real-line to the positive real-line. In literature, the issue of having no strictly negative (or positive when considering flow in the positive direction) the issue of having no **backflow**. In fact, up the moment of writing, no adequate POVM \hat{O}_t (a superset of usual projection-valued measures (PVMs) in quantum mechanics) has been constructed as to produce a strictly positive probability arrival distribution [9]. Even worse, it has been demonstrated that no general POVM \hat{O} exists for which the following holds [10]:

$$\langle \psi_0 | \hat{O}_t | \psi_0 \rangle = j(x = 0, t) \quad (33)$$

In other words, canonical quantum mechanics is foremost a framework for *predicting measurement outcomes*, and therefore, quantum mechanical quantities are not intrinsic parts of the system under study, or independent of the measurement device.

7.3.2. Entering Bohmian Mechanics

Bohmian Mechanics is an alternative theory of quantum phenomena, yet giving the same empirical predictions as canonical quantum mechanics [27] [28]. Both theories share their foundations in the concept of a wave function which obeys the Schrödinger equation. Canonical quantum mechanics has

some further postulates regarding the collapse of the wave function, and how all objects are described by wave functions. Bohmian Mechanics poses that the world around us is composed of real point particles that move alongside continuous pathways, also called **bohmian trajectories**, guided by a guidance wave or **pilot wave**. The latter is determined by the wave equation. The usual quantum mechanical formalism can be recovered from Bohmian mechanics as an effective description of measurement situations.

It's important to state that canonical quantum theory is concerned with **measurement outcomes** whereas Bohmian Mechanics gives an account of the physical reality in a quantum setup. In other words, canonical quantum theory deals with PVMs and POVMs exclusively, whereas even though Bohmian mechanics predicts the same outcome, they're not the main focus of the bohmian view.

In non-relativistic quantum mechanics, a general wave function can be written as

$$\Psi = \sqrt{\rho(\vec{r}, t)} \cdot \exp\left(i \frac{S(\vec{r}, t)}{\hbar}\right) \quad (34)$$

Where $\rho(\vec{r}, t) = \Psi^* \Psi$ the probability density of the wave function, and $S(\vec{r}, t)$ its phase. In Bohmian Mechanics, particles are real (they don't span the whole space) and are *guided* by a **guiding equation** or **pilot wave**. This guiding equation determines a well-defined velocity for every particle passing through a velocity field of the following form:

$$\vec{v} = \frac{\vec{j}(\vec{r}, t)}{\rho(\vec{r}, t)} = \frac{1}{m} \nabla S(\vec{r}, t) \quad (35)$$

Where \vec{j} represents the probability current or **probability flux** of the wave function.

The spatial variation of the wave function characterizes the probability flux of the wave function, and thus also its velocity. Having the velocity equal to $\frac{\nabla S(\vec{r},t)}{m}$ is interestingly a classical limit in fluid dynamics.

The arrival time of a particle in Bohmian Mechanics can be determined by following the motion of a particle's Bohmian trajectory, then registering the time at which the trajectory arrives at detector:

$$\frac{d}{dt} \vec{r}(t) = \vec{v}(\vec{r}(t), t) = \frac{|j(\vec{r}(t), t)|}{|\Psi(\vec{r}(t), t)|^2} \quad (36)$$

$$\Rightarrow \vec{r} = \vec{r}_0 + \int_0^t \vec{v} dt \quad (37)$$

The Bohmian Mechanical velocity of a particle in her domain is not directly related to the quantum mechanical momentum, rather it encodes information about the possible results of possible momentum measures. To obtain the same predictions as canonical quantum mechanics, one ought to *spawn* or start sufficient Bohmian particles at $t = 0$, in a probability distribution that is in accordance with $|\psi(x, t = 0)|^2$, then averaging the arrival times (or arrival positions) across all particles in the ensemble.

The arrival time $\Pi(t)$ can now be interpreted in light of Bohmian Mechanics. Previously, the requirement was to have the momentum of the particle be strictly negative (as in: moving towards the origin from the positive real axis). Now, we require the Bohmian velocity to stay negative after the initial state preparation. When a particle crosses a detector at $x = 0$, the trajectories would have spanned a distance $\vec{v}(x = 0, t)dt$ in a timespan $t + dt$ (see figure 10). This probability to arrive in this region beyond the detector is the distance covered ($\vec{v}(x = 0, t)dt$) multiplied by the probability to find a particle there, $|\psi(x = 0, t)|^2$, which gives a simple equation for the arrival time distribution, with

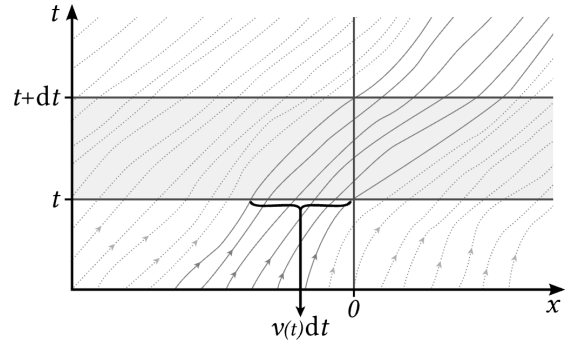


Figure 10: Bohmian trajectories in the vicinity of the detector at $x = 0$. Trajectories that cross the detector cover a distance of $\vec{v}(t)dt$ in a time interval dt . Image from [21].

the minus put in place since we're considering negative velocities in the discussed setup:

$$\Pi(t) = -\frac{d}{dt} |\psi(x = 0, t)|^2 \vec{v}(x = 0, t)dt \quad (38)$$

$$= -j(x = 0, t) \quad (39)$$

This is essentially the same result as in canonical quantum mechanics, however we're now dealing with a physical justification for approaching this problem. What still has to be taken into account is the notion of cross the detector - it's perfectly possible for a bohmian trajectory to cross the detector twice. In these cases, the first crossing is usually taken into account, which is called **truncated current** in literature. Further this approach is readily generalizable to 3 dimensions, and detector shapes \vec{r}_{path} of any kind.

So far in our discussion, potentials in the pathway of the particle are not handled, nor is the modeling of the detector itself ignored, however when including these, the conclusions are generally the same:

The probability density of the arrival time t at a detector $\vec{r}_{\text{detector}}$ is given by:

$$\Pi(t) = -j(\vec{r}_{\text{detector}}, t) \quad (40)$$

iff the bohmian trajectories are strictly positive to one direction across the detector.

In the discussed setup of a particle in free fall across a barrier, this is guaranteed to occur because the linear gravitational potential will always pull a particle down to the negative real axis. Further, by employing finetuned **complex absorption potentials** below the detector, we can ensure that no reflections to the positive directions occur when simulating the experiment. In other words, even though no general POVM exists for modeling adequate probability currents that would correspond with the arrival time at the detector *in general*, in highly specific setups like ours, and by employing adequate numerical techniques, it's still possible to produce meaningful physical results.

7.3.3. Arrival Time for free-falling particles in low energy regimes

Thus far, we held a general discussion about the arrival time. The discussion will now shift towards analysis of the physically realizable setup proposed in the introductory section of this study: a particle at rest is dropped in free fall onto a **delta barrier** at the origin, with a detector place below the origin at a distance $z = -L$ (see setup in figure 2 on page 3).

The Hamiltonian of this setup is given by:

$$i\hbar \frac{\partial}{\partial t} \psi(z, t) = -\frac{\hbar^2}{2m} \frac{\partial^2}{\partial z^2} \psi(z, t) + (\gamma\delta(z) + mgz) \psi(z, t) \quad (41)$$

The length and energy scales of the problem are well-known in literature:

$$\ell_0 = \sqrt[3]{\frac{\hbar^2}{2m^2g}}, \quad E_0 = mg\ell_0, \quad (2)$$

To make analysis of such a system easier, consider the introduction of the following dimensionless quantities:

$$z' = \frac{z}{\ell_0}, \quad t' = \frac{E_0}{\hbar}t, \quad \gamma' = \frac{\gamma}{E_0\ell_0}. \quad (3)$$

which after setting $\hbar = 2m = \frac{g}{2} = 1$, and substituting $\psi \rightarrow \psi'(z', t') = \sqrt{\ell_0}\psi(l_0z', \frac{\hbar}{E_0}t')$ one gets:

$$i\frac{\partial}{\partial t} \psi(z, t) = -\frac{\partial^2}{\partial z^2} \psi(z, t) + (\gamma\delta(z) + z) \psi(z, t) \quad (42)$$

We now focus on the major analytical results proclaimed By Siddhant D. in [16], which calculates the probability current at a plane $z = -L$ through a delta barrier, by assuming far-field detectors ($L \gg 1$), stationary-phase of the wave function, and a low kinetic energy (z_0 is small, ie the particle is dropped from a low height). The solution is an approximate solution using well known Green's function solutions to the posed problem, and making assumptions as to the real part of the associated Propagators when solving the Green's function. The result of the cited paper are summarized in the following box:

$$\Pi_\gamma(\tau) = -J_z(-L, \tau) \quad (43)$$

$$\approx \frac{2\tau \left| \hat{\psi}(L + \tau^2) \right|^2}{1 + (2\pi\gamma)^2 \text{Ai}^4(-L - \tau^2)} \quad (44)$$

where γ is the barrier strength (required to be small in this setup), and L the distance of the detector from the origin, below the origin, and $\hat{\psi}(E)$ is the *Airy Transformed* of ψ_0 :

$$\hat{\psi}(E) = (2\sigma\sqrt{\pi})^{1/2} \exp \left[\frac{\sigma^2}{2} \left(\frac{\sigma^4}{6} + z_0 - E \right) \right] \times \quad (45)$$

$$\text{Ai} \left(\frac{\sigma^4}{4} + z_0 - E \right), \quad (46)$$

and ψ_0 is a generic normalized Gaussian function of width σ , centered at z_0 :

$$\psi(z, 0) = \frac{1}{\sqrt{\sigma}\sqrt{\pi}} \exp \left[-\frac{(z - z_0)^2}{2\sigma^2} + iv_0(z - z_0) \right] \quad (47)$$

This analytical result will be analysed with numerical methods later in this paper.

Note that this analytical solution is only possible because of the delta potential setup, which is principle is not a realistic barrier. Realistic barriers are usually gaussian, which makes them impossible to solve analytically, especially with the linear gravitational potential component in the Hamiltonian.

7.3.4. More on Probability Densities

The probability current J of the wave function Ψ of spinless particles of mass m in 1D is defined as:

$$J = \frac{\hbar}{2mi} (\Psi^* \partial_x \Psi - \Psi \partial_x \Psi^*) \quad (48)$$

$$= \frac{\hbar}{m} \text{Im} (\Psi^* \partial_x \Psi) \quad (49)$$

In 3D, this generalizes to:

$$\vec{J} = \frac{\hbar}{2mi} (\Psi^* \nabla \Psi - \Psi \nabla \Psi^*) \quad (50)$$

$$= \frac{\hbar}{m} \text{Im} (\Psi^* \nabla \Psi) \quad (51)$$

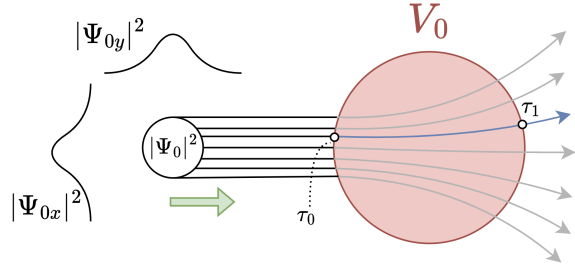


Figure 11: The tunneling time on Bohmian trajectory is defined as $\tau_1 - \tau_0$, respectively the time of entering and exiting the barrier, in case the boundaries of the barrier are well-defined.

For spin-S particles, the probability current obtains an extra field potential term, and a spin-component term, after substituting $\hat{p} = -i\hbar\nabla$:

$$\vec{J} = \frac{1}{2m} \left[(\Psi^* \hat{p} \Psi - \Psi \hat{p} \Psi^*) - 2q\vec{A}|\Psi|^2 \right] \quad (52)$$

For the purposes of this paper, neutral particles will be analyzed, hence $\vec{A} = 0$. The current is sometimes written with the curl of spinor coupling, which is ignored in this text.

7.4. Tunneling Time

In the Bohmian Mechanical picture, tunneling time through a barrier is adequately defined due to the nature of **Bohmian trajectories**, and follows the same argument as for the arrival time in the previous section. Consider the setup as seen in figure 11, where a normalized gaussian wave packet ψ_0 approaches a potential V_0 .

Consider a Bohmian trajectory $\vec{Q}(t)$, which tunnels through the barrier of strength V_0 . The tunneling time of this trajectory equals to $\tau_Q = \tau_1 - \tau_0$, at least if the boundary of the barrier is well-defined. In the discussion section of this paper, it shall be discussed how gaussian barriers have a not well-defined barrier, making the notion of tunneling time inherently ambiguous in the Bohmian picture.

In any case, the average tunneling time of a quantum particle is the average tunnel time of N such Bohmian trajectories, which have been initialized in according to the wave function density distribution $|\psi_0|^2$:

$$\tau_t = \frac{1}{N} \sum_{i=0}^N \tau_1^{(i)} - \tau_0^{(i)} \quad (53)$$

It's important to emphasize that Bohmian trajectories are derived from the probability current \vec{j} , hence for adequate results, *first crossing* of the barrier, and the first exit of the barrier, ought to be brought into consideration. In other words, backflow ought to be eliminated at the time window of tunneling. Numerically this can be solved by setting up complex absorbing potentials around the edges of the simulated domain, or stopping the simulation before the particle has significantly reached the edges of the simulation.

7.5. Larmor Spin Precession And Larmor Clocks

A classical electromagnetic result is that when a dipole is put into a uniform magnetic field B_0 , then the dipole will start precessing at the **Larmor frequency** due to the torque exerted on the dipole moment. This quantity is given by

$$\omega_L = \gamma B_0. \quad (54)$$

This classical result applies to dipoles produced by quantum mechanical spin- $\frac{1}{2}$ particles. For electrons, $\gamma_e = -\frac{e}{2m_e}g_e$, with $g_e \approx 2$, the electron g-factor, and m_e the electron mass. For nuclei, $\gamma_N = \frac{e}{2m_p}g$, with g the nuclear g-factor, and m_p the proton mass. The main idea discussed in this sector is the retrieval of the **tunneling time** τ_t from the spin precession.

Consider a Hamiltonian for a spin- $\frac{1}{2}$ particle with a spin potential component:

$$\hat{H} = -\frac{\hbar^2}{2m} \nabla^2 - \vec{\sigma} \cdot \vec{B} \quad (55)$$

With $\vec{\sigma}$ the Pauli Spin Matrix vector. For simplicity consider a two dimension setup, with the \vec{B} pointing in the positive z-direction. This simplifies the Hamiltonian to

Have a particle Ψ prepared in some arbitrary superposition of spin up ψ_\uparrow and spin down ψ_\downarrow , and assume Ψ to be normalized in the usual fashion:

$$\Psi = \begin{pmatrix} \psi_\uparrow(x, y, t) \\ \psi_\downarrow(x, y, t) \end{pmatrix} \quad (56)$$

As the particle will now evolve over time, the expectation values for Pauli Spin matrices $\langle \sigma_x \rangle$ and $\langle \sigma_y \rangle$ can be calculated,

$$\langle \sigma_x \rangle = \langle \Psi | \sigma_x | \Psi \rangle \quad (57)$$

$$= \frac{\hbar}{2} \iint (\psi_\uparrow^*(x, y, t) \psi_\downarrow^*(x, y, t)) \begin{pmatrix} 0 & 1 \\ 1 & 0 \end{pmatrix} \begin{pmatrix} \psi_\uparrow(x, y, t) \\ \psi_\downarrow(x, y, t) \end{pmatrix} \quad (58)$$

, equivalently for $\langle \sigma_y \rangle$ with $\sigma_y = \frac{\hbar}{2} \begin{pmatrix} 0 & -i \\ i & 0 \end{pmatrix}$. This returns the following two equations for the expectation values:

$$\langle \sigma_x \rangle = \iint [\psi_{\uparrow}^*(x, y) \psi_{\downarrow}(x, y) + \psi_{\downarrow}^*(x, y) \psi_{\uparrow}(x, y)] d^2r, \quad (59)$$

$$\langle \sigma_y \rangle = \text{Im} \iint [\psi_{\uparrow}^*(x, y) \psi_{\downarrow}(x, y) - \psi_{\downarrow}^*(x, y) \psi_{\uparrow}(x, y)] d^2r \quad (60)$$

When dealing with a discretized simulation of partial the TDSE, the spin quantities are obtained by summsing complex amplitudes of the wavefunctions in the following way:

$$\langle \sigma_x \rangle \approx \Delta x \Delta y \sum_{i,j} \left[\psi_{\uparrow}^*(x_i, y_j) \psi_{\downarrow}(x_i, y_j) \right] \quad (61)$$

$$+ \psi_{\downarrow}^*(x_i, y_j) \psi_{\uparrow}(x_i, y_j) \right], \quad (62)$$

and similarly for $\langle \sigma_y \rangle$, with Δx and Δy the grid size of the discretization.

In a weak magnetic barrier, one may expect a shift in phase, accrued inside the barrier region, and hence the precession angle can be approximated by

$$\Theta(t) \approx \tan^{-1} \left(\frac{\langle \sigma_y \rangle}{\langle \sigma_x \rangle} \right). \quad (63)$$

The time returned by the **Larmor Clock** is now a dynamically derived quantity of the time spent in the barrier, given by

$$\tau_{tunneling} = \frac{\Delta \Theta}{\gamma B_0} = \frac{\Delta \Theta}{\omega_L} \quad (64)$$

, which corresponds to Bütticker weak-field expression of the larmor clock [11]. This approximation has been derived by Bütticker for square wells, but he has demonstrated that the approximation holds for any symmetric barriers. In this study we're using the circular

square well, and the Gaussian barrier, both of which are symmetrically placed at the origin. Bütticker original formula states that $\tau = \sqrt{\tau_p^2 + \tau_t^2}$, where τ_p is the spin precession in the xy plane on the Bloch sphere, whereas τ_t^2 is the time it took for the spin states to start mixing - the transversal spin precession. In this study, both symmetric barrieirs, and weak ones are considered, quaranteeing that the spin states are not mixing. Bütticker's Larmor Clock has been critiqued, with a rebuttal posed in [29]. In 2021, another rebuttal came to the forefront by [17], which corresponds with findings in this study.

In this study, the **larmor clock** and **Bohmian tunneling time** are compared and discussed.

Most theory regarding the physics has been discussed and presented. What follows is a series of section regarding numerical simulations of quantum systems.

7.6. The Split Operator Method

This section is concerned with the theoretical aspects of simulation a time dependent schrödinger equation in a discretized fashion, and in particular of a well known method that is both fast and accurate on limited hardware, the **Split Operator Method**, which is a different name for the Strange Splitting method.

Consider the general case of numerically solving a linear equation

$$\dot{y} = L_1(y) + L_2(y) \quad (65)$$

where L_1 and L_2 are linear operators. With associated solution:

$$y = e^{(L_1+L_2)t} y_0 \quad (66)$$

If L_1 and L_2 commute, then by exponential laws, equation 67 simplifies to

$$y = e^{L_1 t} e^{L_2 t} y_0 \quad (67)$$

If L_1 and L_2 don't commute, then by using Baker-Campbell-Hausdorff (BCH) formula,

$$e^{(\hat{X} + \hat{Y})} = e^{\hat{X}} e^{\hat{Y}} e^{\frac{1}{2}[\hat{X}, \hat{Y}]} + \dots \quad (68)$$

one can still split up the solution, with an error $\mathcal{O}(t^2)$:

$$y = e^{(L_1 + L_2)t} y_0 = e^{L_1 t} e^{L_2 t} y_0 + \mathcal{O}(t^2) \quad (69)$$

One may now solve solve the solution iteratively by taking timestep Δt , and applying the linear operators one after another:

$$\tilde{y}_1 = e^{L_1 \Delta t} y_0 \quad (70)$$

$$y_1 = e^{L_1 \Delta t} \tilde{y}_1 \quad (71)$$

$$\tilde{y}_2 = e^{L_1 \Delta t} y_1 \quad (72)$$

$$y_2 = e^{L_1 \Delta t} \tilde{y}_2 \quad (73)$$

The error can be reduced to $\mathcal{O}(t^3)$ by using Taylor Expansions and comparing error terms, whose details are out of scope of this text. The solution involves taking taking *half steps* for either one of the linear operators. An iteration looks as follows:

$$\tilde{y}_1 = e^{L_1 \frac{\Delta t}{2}} y_0 \quad (74)$$

$$\bar{y}_1 = e^{L_2 \Delta t} \tilde{y}_1 \quad (75)$$

$$y_1 = e^{L_1 \frac{\Delta t}{2}} \bar{y}_1 \quad (76)$$

$$\tilde{y}_2 = e^{L_1 \frac{\Delta t}{2}} y_1 \quad (77)$$

$$\bar{y}_2 = e^{L_2 \Delta t} \tilde{y}_2 \quad (78)$$

$$y_2 = e^{L_1 \frac{\Delta t}{2}} \bar{y}_2 \quad (79)$$

This process is called **Strange Splitting**, and it can be easily applied to the time-dependent Schrödinger equation . Consider a wave function $\Psi(\vec{r}, t + dt) = \Psi(t + dt)$ (written without position to save space) over time, in single iteration timesteps dt and a Hamiltonian $\hat{H} = \hat{H}_{kin} + \hat{H}_{pot} = \hat{T} + \hat{V}$. The Strange splitting looks as follows for this method:

$$\Psi(t + dt) = \exp\left(-\frac{i}{\hbar} \hat{H} dt\right) \Psi(t) \quad (80)$$

$$= e^{-\frac{i}{\hbar} \hat{H}_{pot} dt} e^{-\frac{i}{\hbar} \hat{H}_{kin} dt} \Psi(t) + \mathcal{O}(t^2) \quad (81)$$

$$= e^{-\frac{i}{\hbar} \hat{H}_{pot} \frac{dt}{2}} e^{-\frac{i}{\hbar} \hat{H}_{kin} dt} e^{-\frac{i}{\hbar} \hat{H}_{pot} \frac{dt}{2}} \Psi(t) + \mathcal{O}(t^3) \quad (82)$$

The Split Operator Method is the name given the process where equation 82 can be quickly and efficiently iterated upon using Fast Fourier Transforms (FFT). In quantum mechanics, the fourier transformation of the wavefunction transforms it into **momentum space**, allowing the momentum-space transformed wave function to be efficiently multiplied by $e^{-\frac{i}{\hbar} \hat{H}_{kin} dt}$. The whole process involves multiplying the wave function's complex amplitudes by the Strange Splitted Hamiltonian in equation 82, with FFT and iFFT inbetween the *potential half steps*. The Split Operator Method looks as following:

$$\Psi(z)|_t \quad (83)$$

$$\xrightarrow{\text{Potential Half Step}} \Psi(z) \times e^{-\frac{i}{2\hbar} \hat{V}(z) dt} \quad (84)$$

$$\xrightarrow{\text{FFT}} \tilde{\Psi}(k) \quad (85)$$

$$\xrightarrow{\text{Kinetic Step}} \tilde{\Psi}(k) \times e^{-\frac{i}{\hbar} \hat{H}_{kin} dt} \quad (86)$$

$$\xrightarrow{\text{Inverse FFT}} \Psi(z) \quad (87)$$

$$\xrightarrow{\text{Potential Half Step}} \Psi(z) \times e^{-\frac{i}{2\hbar} \hat{V}(z) dt} \quad (88)$$

$$\Psi(z)|_{t+dt} \quad (89)$$

Since the FFT and iFFT have been adequately optimised, the split operator method is not only accurate, but incredibly fast.

The Split Operator Method generalizes readily to multiple dimensions, although for this 2 dimension or 3 dimensional FFT ought to be used before applying the kinetic step. Furthermore, this numeric methods requires that the grid space be small enough, such that the discretized momenta in k-space are adequately applied, depending on the barriers and potentials present in the setup.

The Split Operator Method is also easily applied to simulations of spin- $\frac{1}{2}$ particles, where Ψ is then represented by a Pauli spinor. This is discussed in the next section.

7.7. Yoshida's Composition Method - Fourth Order Accuracy

For some applications and simulations, the local errors of the Strange splitting method of order dt^3 are too big, and fourth-order accurate methods are desirable. Y. Yoshida [14] developed a method for constructing higher-order symplectic integrators, composed of several second-order steps. For completion it's worth mentioning that the 4th order extension of the Strange method is attributed to **Forest-Ruth**. In either case, a second order step looks like:

$$U(t) = e^{-i\frac{t}{2}\hat{V}} e^{-it\hat{T}} e^{-i\frac{t}{2}\hat{V}} \quad (90)$$

Yoshida's method prescribes the following composition:

$$U_4(\Delta t) = U(p_1 \Delta t) U(p_2 \Delta t) U(p_1 \Delta t) \quad (91)$$

Where the coefficients p_1 and p_2 are to satisfy

$$2p_1 + 2p_2 = 1 \quad (92)$$

$$2p_1^3 + p_2^3 = 0 \quad (93)$$

and are chosen such that the leading error terms cancel. This method produces symplectic integrators (volume and surface preserving in phase space). A common choice in literature is:

$$p_1 = \frac{1}{2 - 2^{1/3}}, \quad p_2 = -\frac{2^{1/3}}{2 - 2^{1/3}} \quad (94)$$

This construction cancels the third-order error terms, yielding a local error of order Δt^5 and a global error scaling as Δt^4 . The fourth order Yoshida's method will be used to assess the adequacy of employed computation models for arrival and tunneling time.

Note: On Yoshida Method The previously discussed method can be further extended to 6th and 8th order accuracy, using Yoshida's Recursive method. The $\mathcal{O}(dt^8)$ contains 15 Strange steps with carefully chosen coefficients to cancel out higher order errors. This is out of scope of this study, but could be conducted for further testing to ensure high accuracy of leading terms.

7.8. Complex Absorption Potentials

As mentioned at the start of this section, to ensure positive probability current flow in the studied free fall setup beyond Gaussian potentials, it's vital to absorb the wave function at the edges of the simulated domain, and ensure no reflections back up the detector, causing backflow. A first attempt to absorbing the wave function uses Gaussian attenuation masks at about 30% of the edges of the simulation. This approaches causes a lot of reflections. The state-of-the-art approach towards absorbing wave functions is by sing Complex Absorption Potentials, which are of the form

$$-iW(\vec{r}), \quad (95)$$

which is added to the Hamiltonian

7.8.1. Polynomial Complex Absorbing Potential (CAP)

A simple power-law CAP that turns on smoothly inside an absorbing layer of width L at each box edge:

$$W(x) = \begin{cases} \eta(\xi/L)^n, & \xi > 0, \\ 0, & \xi \leq 0, \end{cases} \quad (96)$$

$$\text{with } \xi = \begin{cases} x_{\min} + L - x, & x < x_{\min} + L \\ x - (x_{\max} - L), & x > x_{\max} - L \end{cases} \quad (97)$$

Here $\eta > 0$ is the strength, $n \geq 2$ the even polynomial order, and L the physical thickness of the absorbing strip. Increasing n steepens the profile and reduces low-energy reflection roughly as $R \propto L^{-(2n-2)}$. (Adapted from Feit, Fleck & Steiger - [30].)

In literature, plenty more CAPs can be found, like Gaussian CAPS (didn't work well the setup of this study), Manolopoulos Transmission-Free CAP (TFAP), Riss-Meyer Reflection-Free CAP (RF-CAP), or Smooth Exterior-Scaling (SES) CAP. These have been quickly tested and assessed. It has been concluded that for the use case of this study, the polynomial CAP works very well, when the parameters are well chosen.

7.9. Spectral Derivation

In the spectral method, spatial derivatives are computed by transforming the wavefunction into Fourier space, where differentiation becomes a simple multiplication operation. Suppose $\psi(x, y)$ is defined on a discrete grid. Taking its Fast Fourier Transform (FFT) yields $\tilde{\psi}(k_x, k_y)$, the representation in wave number space. Differentiation with respect to x and y then becomes:

$$\frac{\partial \psi}{\partial x} \longleftrightarrow ik_x \tilde{\psi}(k_x, k_y), \quad (98)$$

$$\frac{\partial \psi}{\partial y} \longleftrightarrow ik_y \tilde{\psi}(k_x, k_y) \quad (99)$$

After this multiplication, applying the inverse FFT retrieves the spatial derivatives:

$$\frac{\partial \psi}{\partial x} = \mathcal{F}^{-1} [ik_x \tilde{\psi}(k_x, k_y)], \quad (100)$$

$$\frac{\partial \psi}{\partial y} = \mathcal{F}^{-1} [ik_y \tilde{\psi}(k_x, k_y)] \quad (101)$$

This approach is highly accurate for periodic or smoothly truncated domains and avoids the finite-difference approximations typically used in grid-based methods. Using spectral derivation was pivotal to computing Bohmian Trajectories for relative small grid-sized.

7.10. 1D Simulations

In order to confront the analytical estimates with fully dynamical data, a one-dimensional time-dependent Schrödinger equation is solved on a finite spatial grid $z \in [x_{\min}, x_{\max}]$ using the split-operator propagator already introduced in the previous section. Only the elements specific to the present free-fall setup are summarized below.

Spatial discretization. The coordinate axis is discretized by a uniform mesh $z_j = x_{\min} + j \Delta z$, $j = 0, \dots, N_x - 1$ with $\Delta z = (x_{\max} - x_{\min})/N_x$. Derivatives entering the kinetic phase factor are evaluated in momentum space through the discrete Fourier transform, $k_j = 2\pi j/(N_x \Delta z)$, but in practice through the Fast Fourier Transform. Kinetic factors are calculated upfront for the discretized spatial grid, allowing for quick simulation times.

External potential. The total potential consists of a linear gravitational term, a tunable barrier at the origin, and an optional complex absorbing part,

$$V(z) = mgz + V_{\text{bar}}(z) - iW(z), \quad (102)$$

where $m = g = \hbar = 1$ in the simulation's natural units.

Barrier. Two barrier models are implemented in the simulation:

$$V_\delta(z) = \alpha \frac{\exp[-(z - z_0)^2/2\sigma^2]}{\sqrt{2\pi}\sigma}, \quad \sigma = \frac{1}{2}\Delta z, \quad (\text{"delta"})$$

$$V_g(z) = V_0 \exp[-(z - z_0)^2/2\sigma^2], \quad (\text{"gaussian"})$$

where the first line approximates an ideal δ -barrier by a narrow Gaussian whose width is tied to the grid spacing.

Absorber. At the simulation boundaries a complex absorbing potential $W(z) \geq 0$ (or, equivalently, a multiplicative mask) suppresses unphysical reflections, enabling long propagation times with modest box sizes. Grid searches for the polynomial CAP are employed for the CAP's free parameters width (absorption layer width), η (absorption), and n (degree). See section 7.8.1 on page 26 for more information. Making the simulation space large enough, employing a width of at least 30% of that of the simulated space, together with a large ($\approx 10^3$), work exceedingly well at absorbing all but the most faint complex amplitudes of the wave function (order of $\approx 10^{-8}$).

Initial state. A minimum-uncertainty, normalized Gaussian packet is released from height z_0 with mean momentum p_0 ,

$$\psi(z, 0) = \frac{1}{(2\pi\sigma_0^2)^{1/4}} \quad (103)$$

$$\exp\left[-\frac{(z - z_0)^2}{4\sigma_0^2} + \frac{i p_0}{\hbar}(z - z_0)\right]. \quad (104)$$

For all experiments conducted in this study, p_0 has been set to 0.

Time stepping. For each interval Δt the state is advanced according to

$$\psi(t + \Delta t) = e^{-\frac{i}{2\hbar}V\Delta t} \quad (105)$$

$$\mathcal{F}^{-1}[e^{-\frac{i\hbar k^2}{2m}\Delta t} \mathcal{F}[\psi(t)]] e^{-\frac{i}{2\hbar}V\Delta t}, \quad (106)$$

or, when higher accuracy is desired, by the fourth-order Yoshida composition of these split steps.

Recorded observables. At each step we store the probability density $|\psi(z, t)|^2$, the cumulative absorbed norm, and the raw complex amplitudes of the wave function using NumPy's 128-bit Complex Value Type. The local probability current required for the arrival-time distribution per unit time is evaluated as

$$j(z, t) = \frac{\hbar}{m} \operatorname{Im}[\psi^*(z, t) \partial_z \psi(z, t)]. \quad (107)$$

All numerical data shown in the remainder of this work are obtained with the above scheme using $N_x = 2048$, $\Delta t = 10^{-3}s$, and box limits $x_{\min} = -40$, $x_{\max} = 40$, in dimensionless units, unless stated otherwise.

Plotting. For plotting, the python library `matplotlib` is used.

For 2-dimensionalal simulations of the same kind (without spin), the setup remains largely the same.

7.11. 2D Simulations with Spin

The setup for modeling Gaussian spin- $\frac{1}{2}$ particles falling under free fall throughout a magnetic is modelled by propagating a two-component spinor $\Psi(\mathbf{r}, t) = (\psi_\uparrow(\mathbf{r}, t), \psi_\downarrow(\mathbf{r}, t))^T$, $\mathbf{r} = (x, y)$, under a Hamiltonian that separates into kinetic and

spin-dependent potential parts,

$$\hat{H} = \underbrace{\left[-\frac{\hbar^2}{2m} (\partial_x^2 + \partial_y^2) \right]}_{\hat{T} \otimes \mathbb{1}_{2 \times 2}} \quad (108)$$

$$+ \underbrace{\left[V_0(\mathbf{r}) \mathbb{1}_2 + V_B(\mathbf{r}) \sigma_z \right]}_{\hat{V}(\mathbf{r})} \quad (109)$$

where $V_0(\mathbf{r}) = mg y$ is the spin-independent gravitational term and $V_B(\mathbf{r})$ is a magnetic barrier that couples to the Pauli matrix σ_z . With the barrier centered at, (x_0, y_0) , a Gaussian profile is used for modeling a physically realistic laser profile

$$V_B^{(G)} = V_0^B \exp[-(\rho/\sigma)^2/2], \quad (110)$$

$$\rho^2 = (x - x_0)^2 + (y - y_0)^2, \quad (111)$$

or, in the second situation, a hard-edged circular uniform magnetic field B_0 . Both situations will be compared regarding the notion of tunneling time.

Split-operator step. At every time increment Δt the state is advanced by the second-order factorization

$$U(\Delta t) = e^{-\frac{i}{2\hbar} V \Delta t} e^{-\frac{i}{\hbar} T \Delta t} e^{-\frac{i}{2\hbar} V \Delta t}, \quad (112)$$

applied as

$$\Psi(\mathbf{r}, t + \Delta t) = U(\Delta t) \Psi(\mathbf{r}, t) \quad (113)$$

with

$$e^{-\frac{i}{2\hbar} \hat{V} \Delta t} = \begin{pmatrix} e^{-\frac{i}{2\hbar} (V_0 + V_B) \Delta t} & 0 \\ 0 & e^{-\frac{i}{2\hbar} (V_0 - V_B) \Delta t} \end{pmatrix}, \quad (114)$$

and

$$e^{-\frac{i}{\hbar} T \Delta t} = \exp\left[-\frac{i\hbar(k_x^2 + k_y^2)}{2m} \Delta t\right] \mathbb{1}_{2 \times 2} \quad (115)$$

after transforming to momentum space $(k_x, k_y) = 2\pi(j_x/N_x \Delta x, j_y/N_y \Delta y)$. The matrix in (114) acts pointwise in real space; its diagonal form means that spin-up and

spin-down amplitudes merely acquire opposite phases, hence **no spin mixing occurs**, which would require keeping track of the Transversal Spin Precession of the Larmor clock, as proposed by the original Büttiker paper.

Explicit component-wise action. Writing out the full 2×2 multiplication for the potential half step makes the algorithmic structure transparent:

$$\begin{pmatrix} \psi_\uparrow \\ \psi_\downarrow \end{pmatrix} \xrightarrow{V} \begin{pmatrix} e^{-\frac{i}{2\hbar} (V_0 + V_B) \Delta t} \psi_\uparrow \\ e^{-\frac{i}{2\hbar} (V_0 - V_B) \Delta t} \psi_\downarrow \end{pmatrix}. \quad (116)$$

After the kinetic FFT step (common to both components) the same matrix is applied once more, completing the single-time-step propagation.

Initial state and observables. The simulation starts from an equal superposition

$$\Psi(\mathbf{r}, 0) = \frac{1}{\sqrt{2}} \psi_0(\mathbf{r}) (1, 1)^T \quad (117)$$

with a minimum-uncertainty packet

$$\psi_0 = (2\pi\sigma^2)^{-1/2} \times \quad (118)$$

$$\exp\left[-\frac{(\mathbf{r} - \mathbf{r}_0)^2}{4\sigma^2} + \frac{i\mathbf{p}_0 \cdot (\mathbf{r} - \mathbf{r}_0)}{\hbar}\right] \quad (119)$$

where \mathbf{p}_0 is set to zero in all discussed simulations in this study. At every stored step, the spin-resolved probabilities $P_{\uparrow,\downarrow} = |\psi_{\uparrow,\downarrow}|^2$ and raw complex amplitudes of the wave function are stored using NumPy's 128 bit complex number type.

For 2D simulations, the number of memory required to complete a successful iteration grows exponentially. A discretization of $Nx = Ny = 512$ at a $\Delta t = 0.01s$ for a space of $x, y \in \mathbb{R}^2$ limited to $[-20, 20]$ worked well for producing physically feasible simulations. The explored free parameter space explored in this study is listed:

- Magnetic Barrier Strength $B_0 \in \{0.5, \dots\}$

- Magnetic Barrier Width - $\sigma = 2$
- Magnetic Barrier Type - Gaussian and Hard-Edged Uniform Circle
- Number of steps = 300
- Drop height = 15 units
- Particle at rest, $p_{0x} = p_{0y} = 0$

7.12. General Workflow

In this section, a brief overview of numeric workflows are laid out, such that it's better understood how to reproduce the results in the next section.

First, Siddant Das [16] low energy regime model for the arrival time distribution is compared with the setup numerical simulations.

After this, the arrival time density for 1-dimensional simulations is analyzed for different barrier strengths, different drop heights, and the tunneling behavior is characterized. For 1 dimension simulations, the calculated space across 50+ simulations can be held into memory. The arrival time results generally translate to two and even three dimensional results, if spin is excluded from the calculation.

Next up, tunneling time is analysed in the **Larmor Clock** theory and Bohmian Theory. For this, two magnetic barrier types are tested at different strengths (circular and Gaussian magnetic uniform barriers). The simulation is ran for 3 seconds, until the wave function hits the barrier. The simulated setup can be seen in figure 2 on page 3. For two dimensional modeling and layering, each simulation data needs to be stored separately on file ($\approx 6.5 \text{ Gb}$ per file), requiring about 450Gb in storage for storing all 2D simulations made in this study. This storage space is readily available in the commercial laptop range. A single 2d simulation run takes 15-25 minutes, depending on available CPU and RAM resources, and simulation parameters. The general workflow for gathering quantities

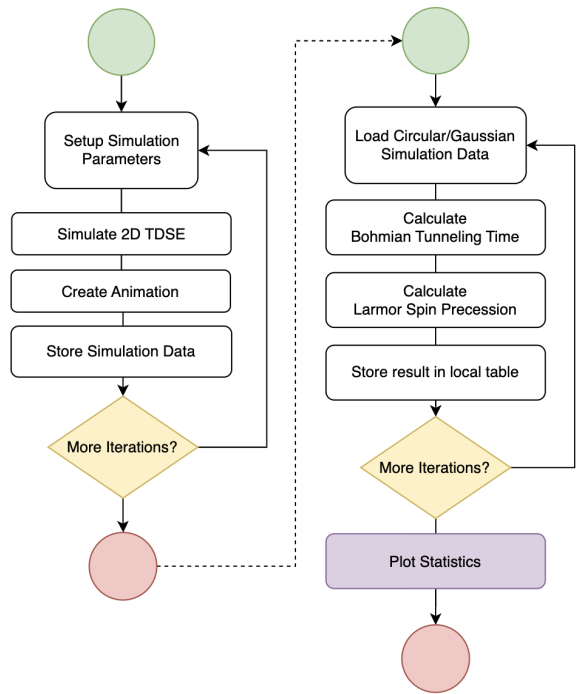


Figure 12: General process for arrival time and tunneling time statistics

across many simulations is depicted in figure 12.

8 APPENDIX B - MORE FIGURES

This section contains supplementary figures and graphics produced during this study, which help give visual context for the discussed material in the main content, and Appendix A.

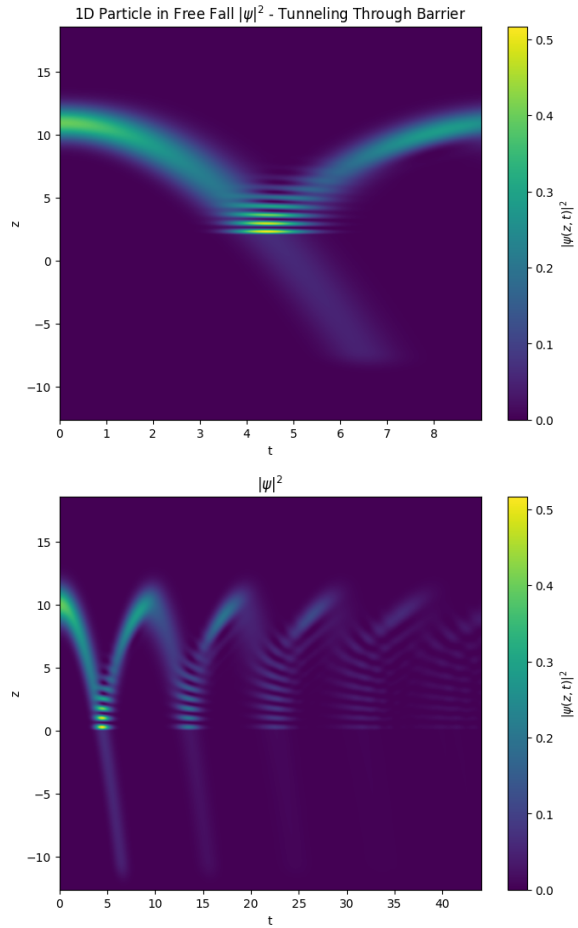


Figure 13: The quantum particle falling under free fall, the transmitted component is absorbed at the boundary of the simulation. The reflected part of the wave function falls back down to the barrier. A detector is placed at $z = -L = -5$

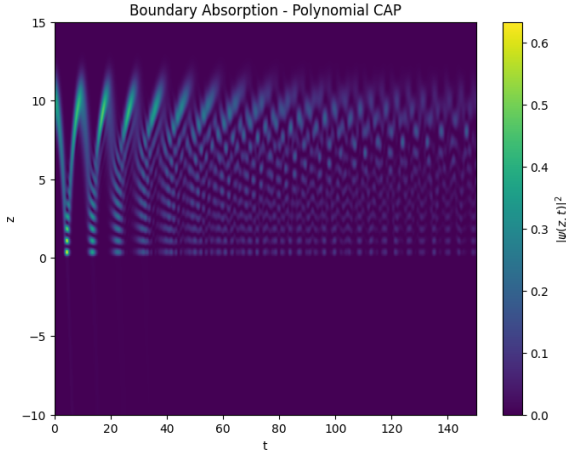


Figure 14: A long-term run, with optimized boundary absorption coefficients, showing diffusion into a particle in a box situation, confined by a triangular barrier on one side.

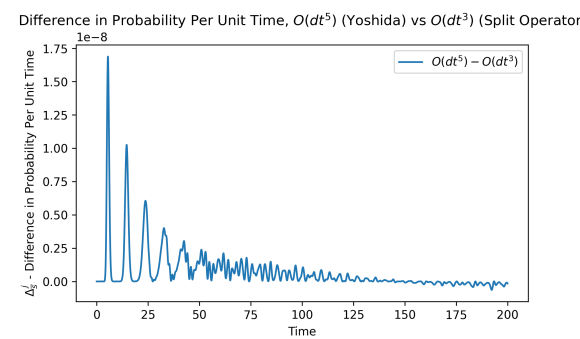
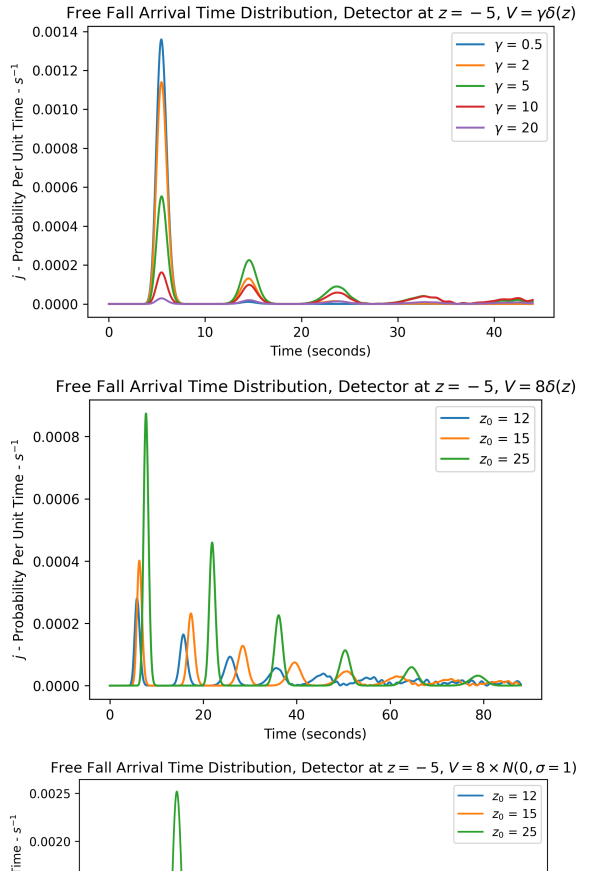


Figure 15: Difference in arrival time between $\mathcal{O}(dt^3)$ and $\mathcal{O}(dt^5)$ methods

Figure 16: Arrival Time Distribution with a $\gamma\delta$ barrier, at different gamma barrier strengths. There's a clear regularity to be spotted here, that's not observed with Gaussian barriers.

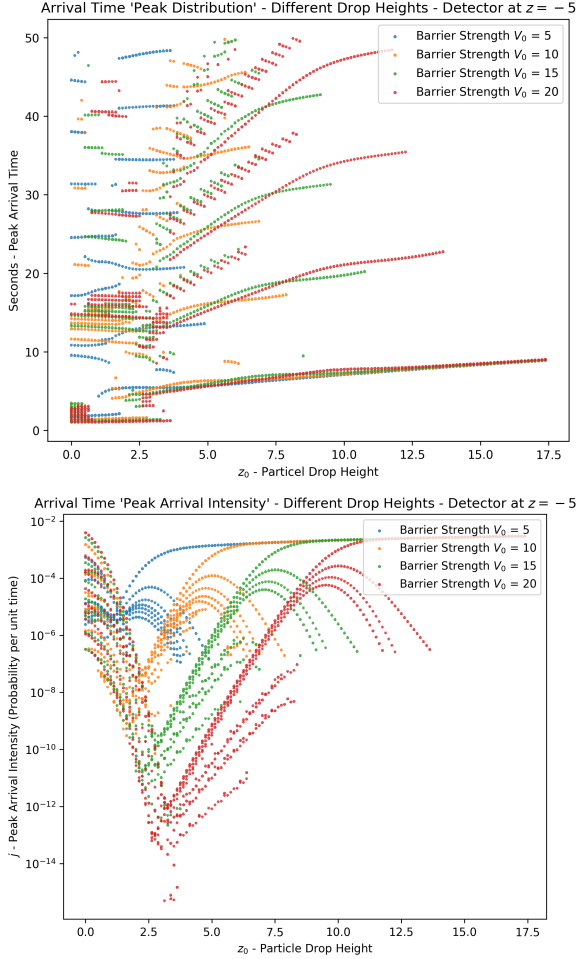


Figure 17: Peaks in Arrival Time Distribution. Each experiment is done at different drop heights (x-axis), and colored according to different barrier strengths. Notice the "continuous" and "chartered" regions in the upper graph starting from drop height 5, and 15 and 20 magnetic units. On the lower graph, notice the asymptotic behaviour of intensity of the first bounce, and the parabola-like drop-off for each subsequent bounce as the particle is dropped from higher heights.

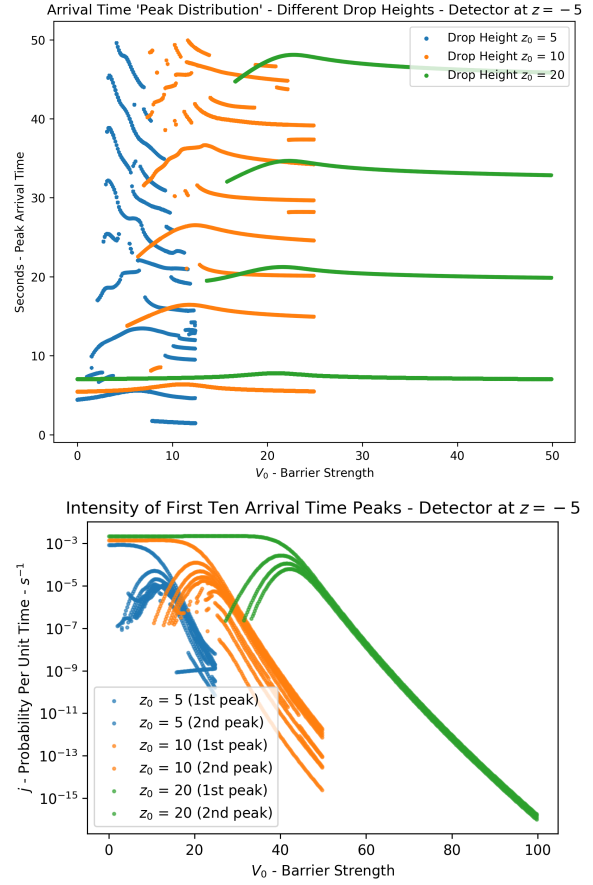


Figure 18: Peaks in Arrival Time Distribution for Gaussian barriers. Each simulated experiment is done at different barrier strength (x-axis), and colored according to different drop heights. The upper chart plots arrival times (seconds) in function of barrier strength, whereas the lower chart plots arrival time intensities in function of barrier strength. Notice the band structure formation in the low barrier strength region on the upper graph. On the lower graph, notice the asymptotically decreasing intensity as the strength of the barrier increases.

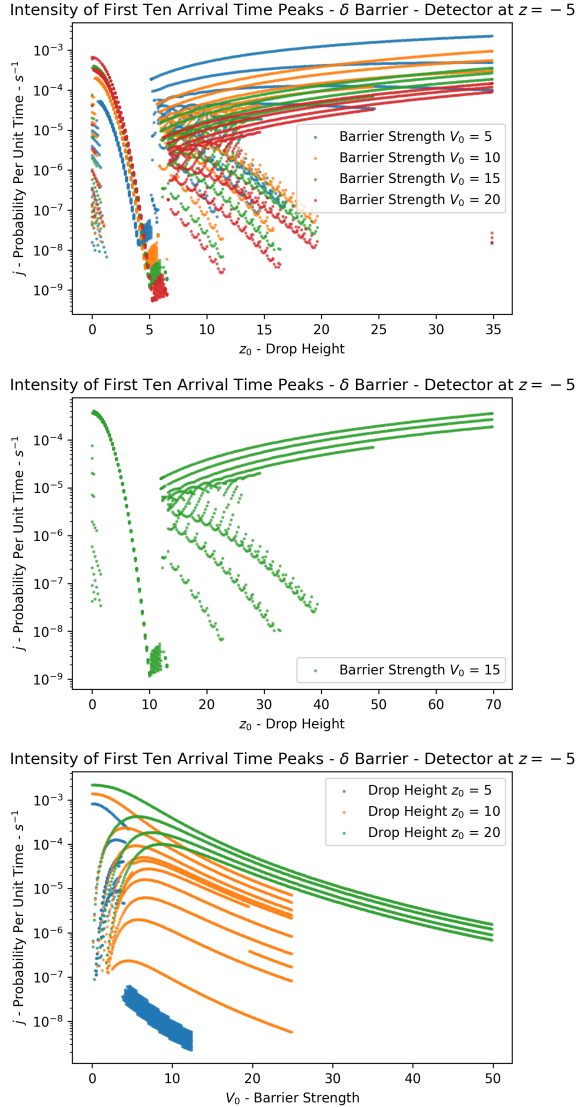


Figure 19: Peaks in Arrival Time (**Intensity**) Distribution for a Delta barrier. Notice the regularity of arrival intensities above 5 drop units in the upper chart making the delta barrier seem to approximate to semi-classical predictions which need further theoretical considerations. On the lower graph, it's clearly seen that regardless of barrier strength, the four situations produce the same peak distribution in seconds, except for the transitional region at 5 units in drop height.

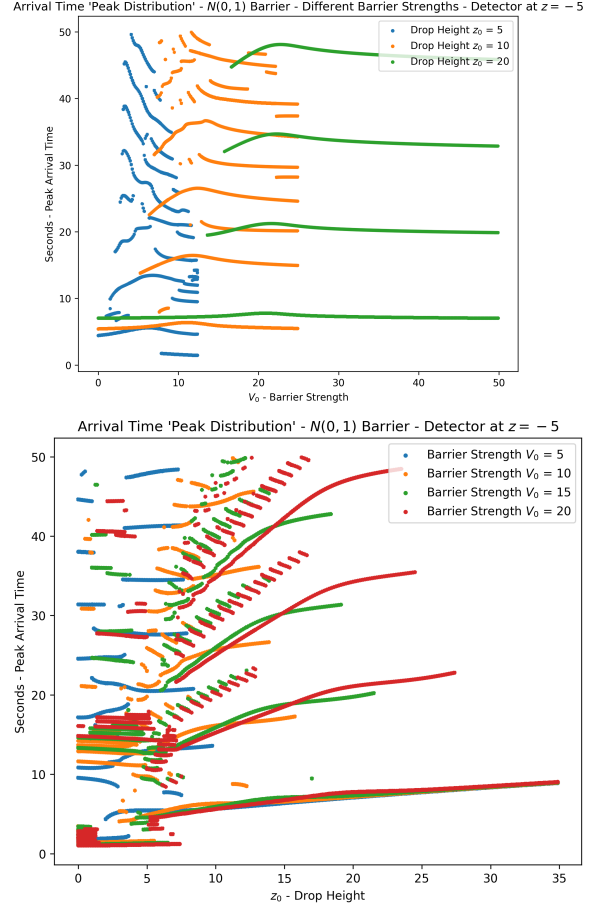


Figure 20: Peaks in Arrival Time (**seconds**) Distribution for a Gaussian barrier. Notice the highly non-trivial of arrival times above 5 drop units. There are, however, discernable features to be recognized. The upper figure features band-formation in the (10,42) region, and show cases tunnelling resonances when observing the peaks of the green arrival times: semi-stable standing waves seems to be created at adequate energies (drop heights) causing the particle to arrive later than anticipated. Upon subsequent reflections, the particle loses energy in a non-linear way, which contributes to the non-linear arrival time distribution. On the lower figure, it's of considerable interest to notice the clearly "continuous" arrival time, and the "broken" odd arrival time.

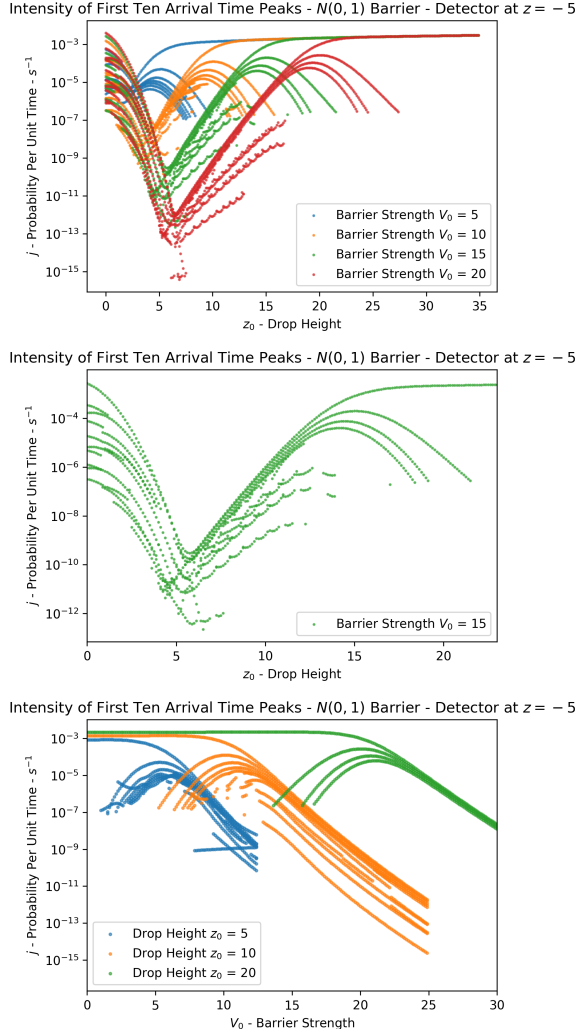


Figure 21: Peaks in Arrival Time (**Intensity**) Distribution for a Gaussian barrier, in function of drop height and barrier strength. Interesting non-linear features can be observed. What's noticeable is the parabola-like formation of the intensity curves of the non-first arrival times, while asymptotically coming closer to one other for higher barrier strengths. On the upper graph, all arrival intensities seem to coincide before they spread, which could be properly characterized and treated theoretically.

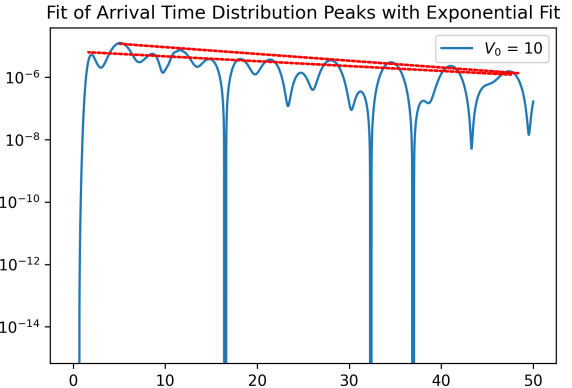


Figure 22: Multiple Characterization possibilities when fitting arrival time peaks. Using a normal `scipy.peaks` function, all peaks would be identified, not distinguishing those "coming up from below" (primary reflections), and those who are "on top" (secondary reflections and quasi-stable wave formation in the barrier). Further work needs to be conducted.

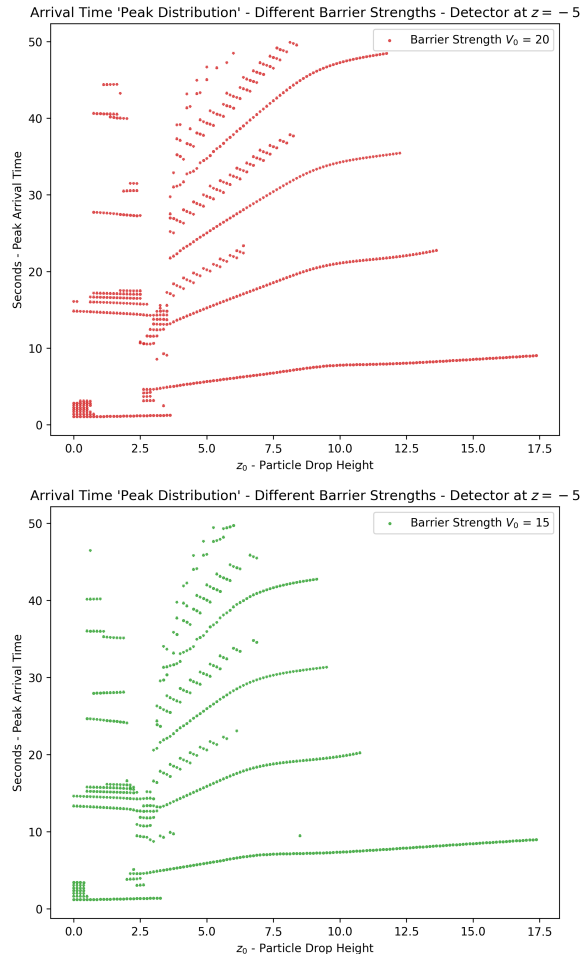


Figure 23: Peaks in Arrival Time (**seconds**) in Gaussian barriers for isolated cases, demonstrating the non-linear effects of the simple setup.

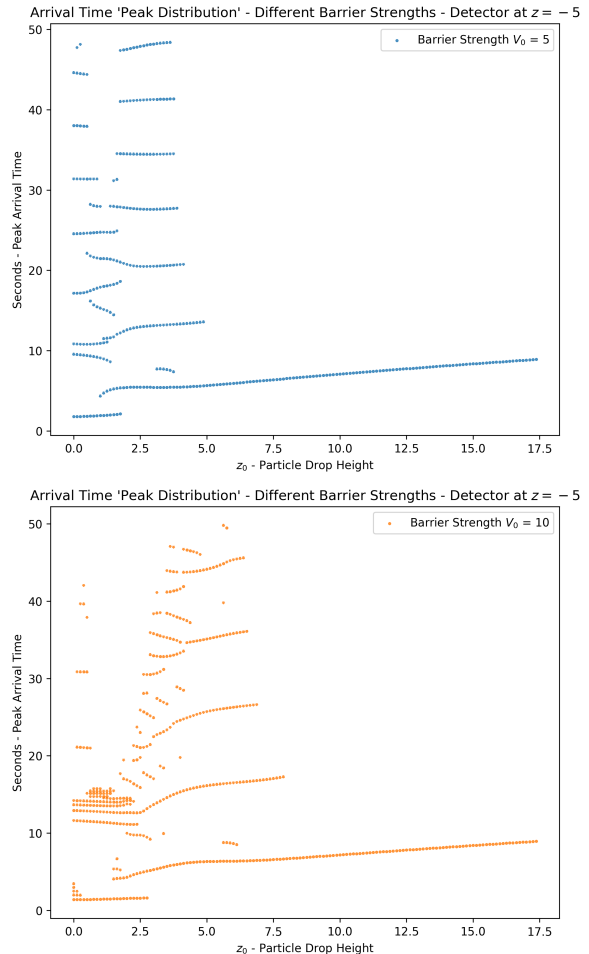


Figure 24: Peaks in Arrival Time (**seconds**) in Gaussian barriers for isolated cases, demonstrating the non-linear effects of the simple setup.

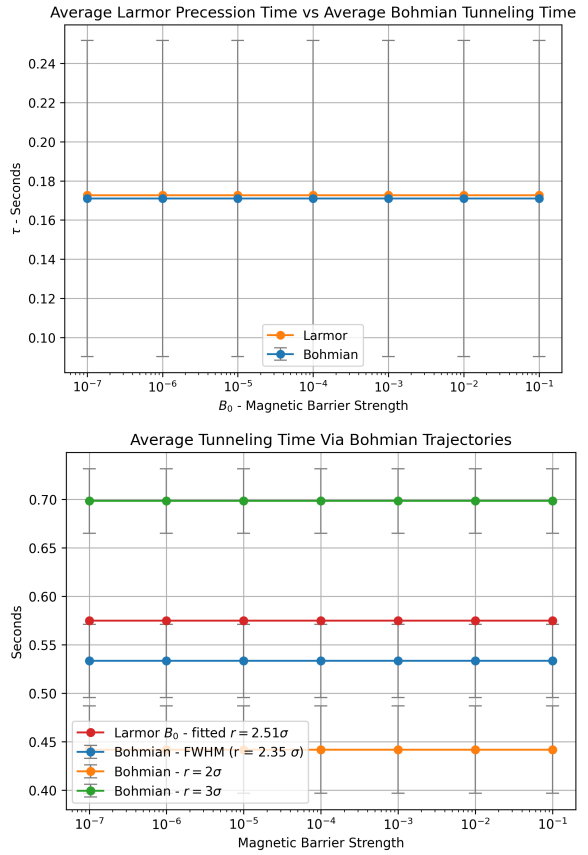
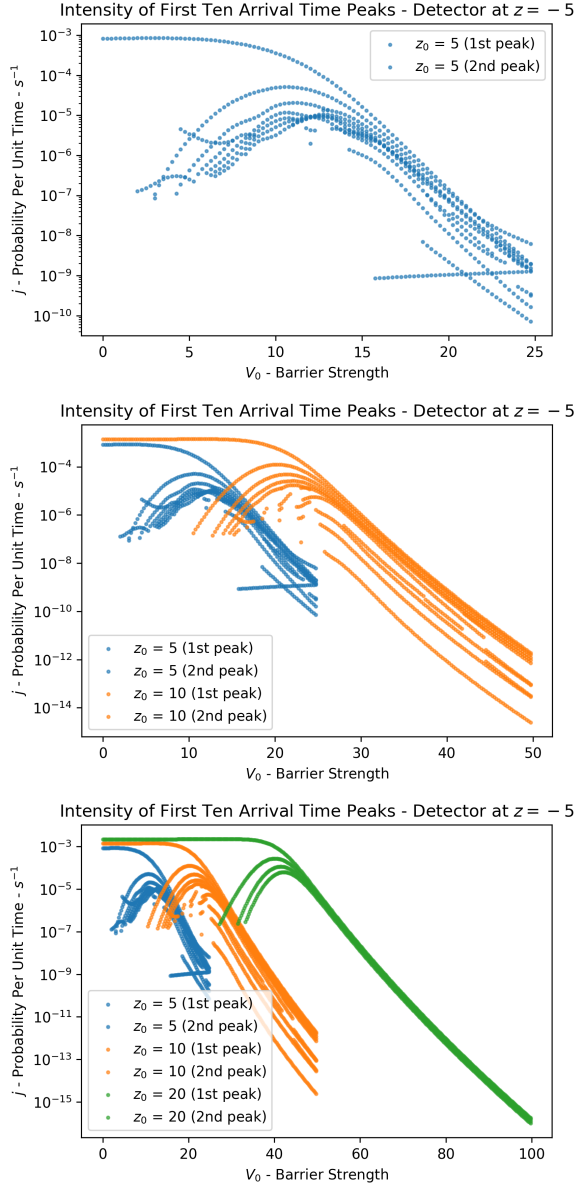


Figure 25: Peaks in Arrival Time (**Intensity**) Distribution, already shown before, here displayed in individually highlighted cases. On the upper graph, notice this particular "weaving" of the fourth arrival (count from top) at coordinate $(12; 7 \times 10^{-6})$ for the blue region. A clear resonant point is forming there, as in all other barrier strengths, multiple arrival time peaks have been witnessed.

Figure 26: Tunnelling Times For a Circular Uniform Barrier with a clear boundary (a), and a guassian barrier (b) both using Larmor Precession Times τ_L , and bohmian trajectories. These data points are obtained in the weak field regime. At low magnetic strengths, the two seem to coincide. Error bars on the Bohmian tunnelling time represent 1 standard deviation.

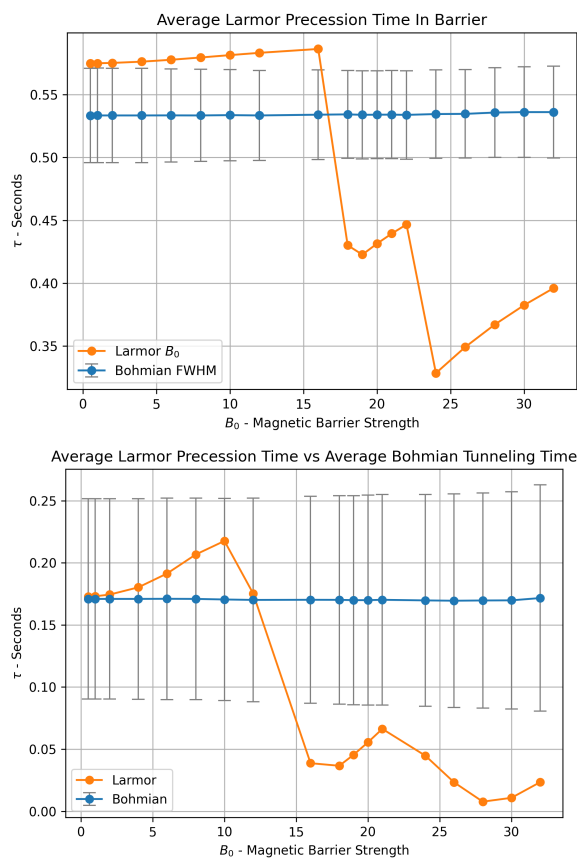


Figure 27: Larmor Clock vs Bohmian Trajectories in strong magnetic field regime. Upper graph shows **gaussian barrier** tunneling times, with $2R = 2 \ln(2) \sigma$ (FWHM). Interestingly, the Bohmian tunneling time seem stable throughout, whereas the Larmor Clock quickly goes out of tilt. The lower figure shows the tunneling times for a circular (square-like) barrier. Here the tunneling times coincide in the low barrier strength regime (which is discussed in the main text of this study)

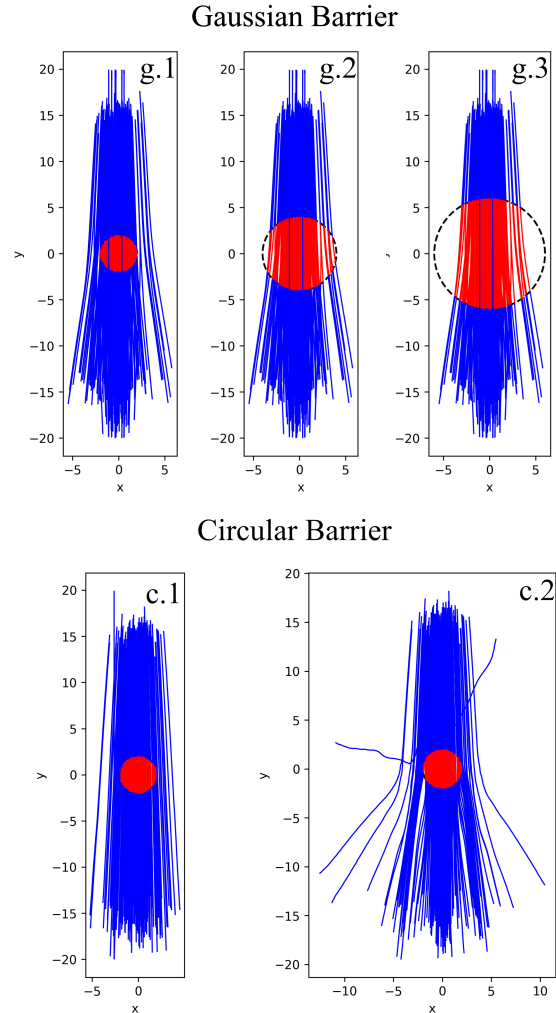


Figure 28: Bohmian Trajectories for Gaussian (g) and circular pathways (c). Parts of the pathways that are falling within the barrier are colored red. Gaussian barriers have well defined boundary. Portrayed are boundaries equal to $2R=[1\sigma, 2\ln(2)\sigma, 3\sigma]$, respectively for [g.1, g.2, g.3]. $2\ln(2)\sigma$ corresponds to FWHM of the laser beam intensity profile.

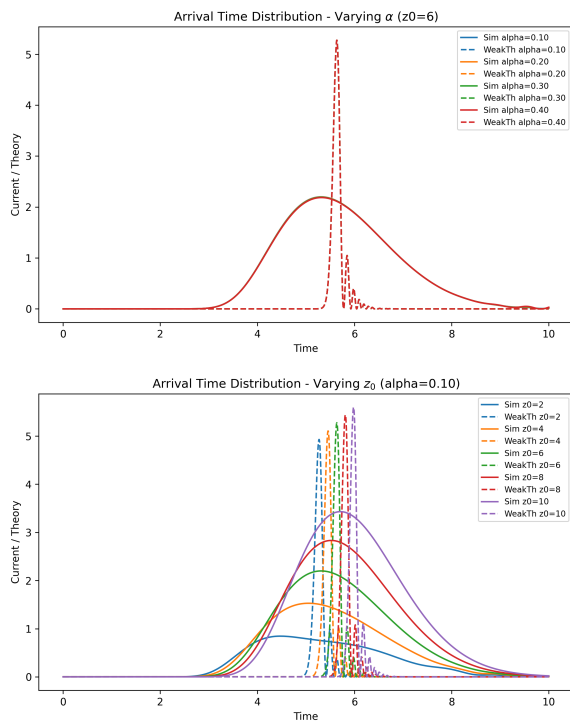


Figure 29: Comparing Weak Barrier Theory vs Bohmian Simulations. The overall "bulk" of the arrival time matches, but the resonant peaks are nowhere to be seen. Further, the peaks for the weak theory don't spread out on the x-axis (time) as the particle is dropped from a higher height, which is to be expected from the general form of the TDSE.

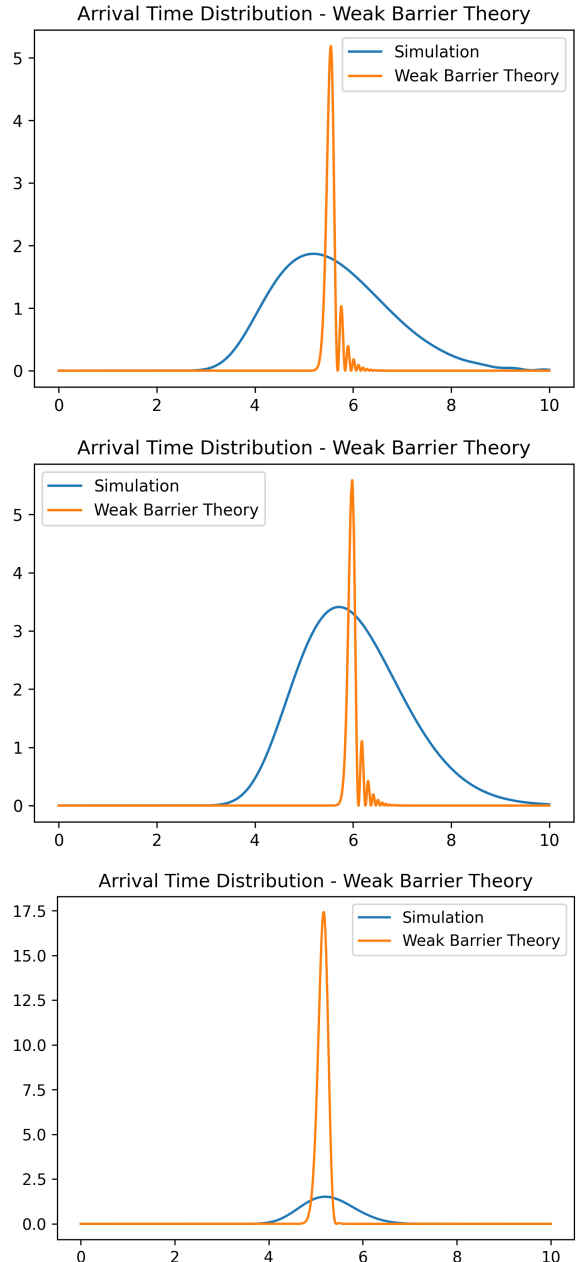
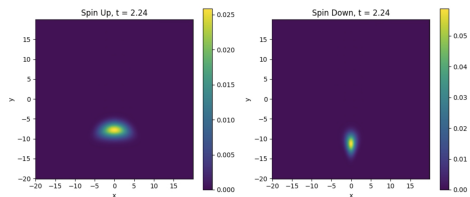


Figure 30: Comparing Weak Barrier Theory vs Bohmian Simulations. The overall "bulk" of the arrival time matches, but the resonant peaks are nowhere to be seen. Figures correspond to different barrier strengths, width, and heights, whose absolute values are irrelevant to specify in the current scope.



(a) First snapshot

Figure 31: This figure illustrates how a 2D particle in free fall, made of ψ_{\uparrow} and ψ_{\downarrow} in superposition, across a **strong Gaussian magnetic field** reacts, is deformed. Notice the clearly smooth spread of the wave function, as opposed to Strong Circular Barriers like in 32

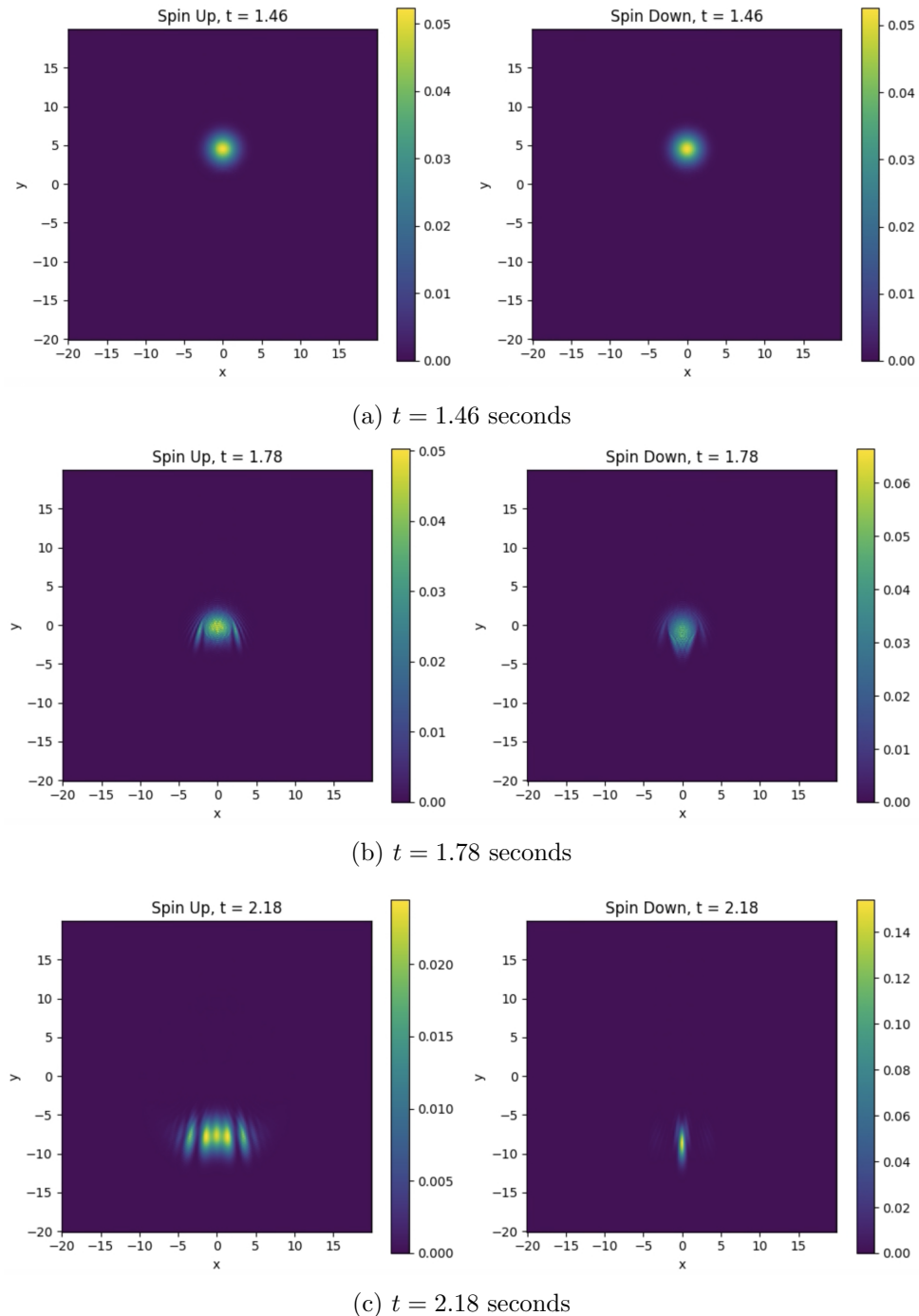


Figure 32: This figure illustrates how a 2D particle in free fall, composed of ψ_{\uparrow} and ψ_{\downarrow} in superposition, across a **strong circular magnetic field**. Both ψ components are plotted separately, respectively left and right. (a-c) shows a time evolution of $|\psi|^2$ for a strong circular barrier, revealing Gibbs Phenomena.